Assessment of Grid-Connected Wind Turbines with an Inertia Response by Considering Internal Dynamics

**Callum Henderson [1], Dimitrios Vozikis [1] , Derrick Holliday [1], Xiaoyan Bian [2] and Agustí Egea-Àlvarez [1,*] **

[1] Power Electronics, Drive and Energy Conversion Group, Electronic and Electrical Engineering Department, University of Strathclyde, Glasgow G1 1XW, UK; callum.henderson.100@strath.ac.uk (C.H.); dimitrios.vozikis@strath.ac.uk (D.V.); derrick.holliday@strath.ac.uk (D.H.)

[2] Electrical Engineering College, Shanghai University of Electric Power, Shanghai 200090, China; bianxy@shiep.edu.cn

*   Correspondence: agusti.egea@strath.ac.uk

check for updates

Abstract: This paper presents a small-signal analysis of different grid side controllers for full power converter wind turbines with inertia response capability. In real wind turbines, the DC link controller, the drivetrain damping controller and the inertial response might present contradictory control actions in a close bandwidth range. This situation might lead to reduced control performance, increased component stress and non-compliance of connection agreements. The paper presents an analysis of the internal wind turbine dynamics by considering different grid-side converter control topologies: standard current control used in the wind industry, standard current control with inertia emulation capabilities and virtual synchronous machines. Comments are made on the similarities between each topology and the negative effects and limits, and possible remedies are discussed. Finally, the conclusion poses that the inclusion of a DC link voltage controller reduces the ability of a converter to respond to external frequency events without energy storage. The degradation increases with the DC link voltage control speed.

Keywords: virtual synchronous machine; inertia provision; DC link voltage control

1. Introduction

The decarbonisation of electrical generation has become a priority to mitigate the effects of climate change [1]. Coal and oil power stations are being replaced by renewable power sources; in the UK in 2019, 35.8% of electricity was generated using renewable technology [2]. Wind, solar and other forms of electric renewable generation are interfaced with a power converter, providing more controllability and flexibility but challenging traditional network operation and control [3]. Wind power is the fastest growing renewable technology and represents the major part of the renewable generated power in Europe [4].

Some studies have shown that the grid may become unstable when power converter penetration surpasses a threshold using standard converter control techniques [5]. The reduction of system inertia has been considered as one of the key factors that might endanger system stability [6]. Several researchers have suggested that the provision of inertia from converter-based systems might be beneficial for the power system [7], but current control, the most popular type of converter control for the integration of renewable power into the grid, cannot support this service. Several approaches have been suggested to improve the converter response during a frequency event, such as adding an inertia loop to a standard current controller [8] or using grid-forming converters [9].

Virtual synchronous machines (VSMs), a particular implementation of a grid forming converter, have drawn great interest in recent years [10–12]. Several topologies have been researched, each with varying complexity, and fall into three main categories: standard vector current control with a synchronous machine outer loop to provide current references [13,14], a full-order synchronous machine with a hysteresis controller or similar [15] and a simplified synchronous machine model using an active power controller to generate a converter angle [16]. The final topology is used in this paper as it provides adequate complexity for studying inertial performance.

A large volume of research has considered the impact of VSM controllers on network stability when the converter under study is connected directly to a suitably large energy source [17–20]. However, literature considering the impact of internal wind turbine dynamics on network stability is limited. This situation can only be analysed with the inclusion of a back-to-back converter, which leads to the necessity of a DC link voltage controller. The location of this controller (network or generator side) can affect the performance of the individual control structures. As the converter attempts to react to an event, the DC link voltage deviates as current is absorbed or injected by the converter. The DC link voltage control attempts to counteract this action and reduces the converter's ability to react. A wind turbine rotor is a promising source of inertia, which is usually decoupled from the grid [21], but with appropriate control, this energy can be produced. However, possible issues arise when the generator-side converter and mechanical properties of the wind turbine are considered. VSMs give a large response at low frequencies that is unaffected in the ideal case. However, certain system components also react at low frequency, such as the algorithm to dampen mechanical oscillations in the drivetrain. These low-bandwidth systems are normally decoupled, but the inclusion of a DC link controller can cause interactions.

This paper presents a model of a full back-to-back converter with a permanent magnet synchronous generator (PMSG) and a two-mass drivetrain. An analysis of the inertial performance of three controllers was performed: a standard vector current controller with inner loop references provided via an active power and voltage loop, the standard current controller with an inertia emulation loop and a VSM controller.

Section 2 discusses the modelling process and adaptions for the small-signal models created to conduct the analysis. Section 3 first describes the model validation process. It then presents the analyses conducted on the DC link controller location, the effect of differing the DC link voltage gains on the generator and network side converter, and finally, the result of using an inertia feedforward to the generator side converter. Section 4 provides a discussion of results and poses further work. Section 5 concludes the paper.

2. Modelling

A grid-connected, full-power converter interfaced wind turbine including the drivetrain is the case under study. Section 2.1 lays out the equations required to model the physical system, while Section 2.2 presents the control structures for the generator side converter and network side converter including the two different types of inertia provision. Finally, Section 2.3 discusses the steps pertaining to the linearisation of non-linear components and other considerations in creating the small-signal model.

2.1. Hardware

To achieve the necessary complexity for analysis, the modelled hardware system included the wind turbine drivetrain, permanent magnet synchronous generator, generator converter, DC link, network converter, converter filter and Thevenin equivalent grid. A diagram of the full system is shown in Figure 1.
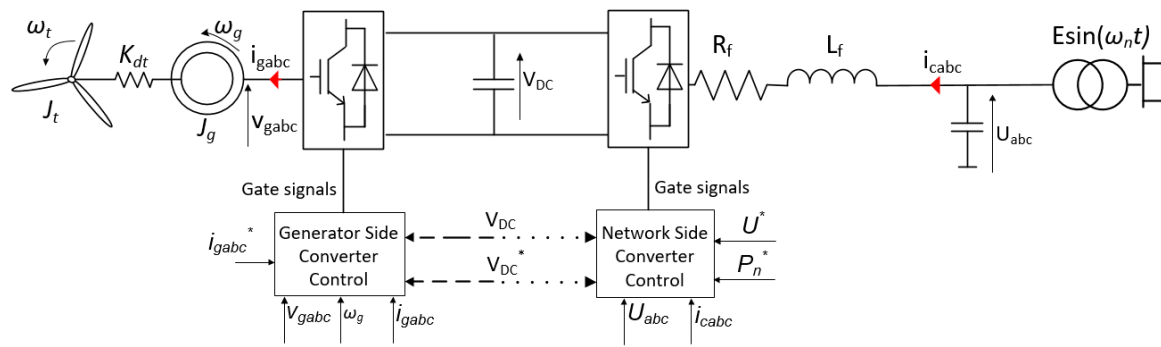
Figure 1. Full model overview.

The drivetrain is modelled as a two-mass system with a flexible shaft to provide the required interactions for study [22,23]. The following equations govern the dynamics, ignoring mechanical losses [24]:

$$\omega_t = \frac{\tau_t - \gamma K_{dt}}{J_t} \tag{1}$$

$$\omega_g = \frac{\gamma K_{dt} - \tau_g}{J_g} \tag{2}$$

$$\gamma = \frac{\omega_t - \omega_g}{s}, \tag{3}$$

where ω_t and ω_g are the turbine and generator rotational speeds, respectively; τ_t and τ_g are the turbine and generator torque, respectively; J_t and J_g are the turbine and generator inertias, respectively; K_{dt} is the flexible shaft stiffness; and γ is the shaft twist angle.

The permanent magnet synchronous generator is modelled in the dq-frame based on [25]:

$$\frac{d}{dt}i_{gd} = \frac{1}{L_{sd}}V_{gd} - \frac{R_s}{L_{sd}} + \frac{L_{sq}}{L_{sd}}p\omega_m i_{gq} \tag{4}$$

$$\frac{d}{dt}i_{gq} = \frac{1}{L_{sq}}v_{gq} - \frac{R}{L_{sq}}i_{gq} - \frac{L_{sd}}{L_{sq}}p\omega_m i_{gd} - \frac{\lambda p\omega_m}{L_{sq}} \tag{5}$$

$$T_e = \frac{3}{2}p\lambda i_{gq} \tag{6}$$

where i_{gd} and i_{gq} are the stator current d and q components, respectively; v_{gd} and v_{gq} are the stator voltage d and q components, respectively; L_{sd} and L_{sq} are the stator inductance d and q components, respectively; R_s is the stator resistance; p is the number of pole pairs; ω_m is the mechanical speed of the generator; T_e is the electromagnetic torque; and λ is the magnetic flux per pole. The model assumes that current into the machine is positive. Therefore, a negative power is used to represent the generating mode. The torque equation was simplified by assuming equal components of d and q inductance.

The network is modelled as a voltage source connected to a Thevenin equivalent impedance. This is the standard approach when considering grid-connected VSCs. The grid side converter is connected to the network via an LC filter. The following equations are used in the model [26]:

$$\frac{d}{dt}i_{nd} = \frac{e_d}{L_n} - \frac{u_d}{L_n} - \frac{R_n}{L_n}i_{nd} - \omega_n i_{nq} \tag{7}$$

$$\frac{d}{dt}i_{nq} = \frac{e_q}{L_n} - \frac{u_q}{L_n} - \frac{R_n}{L_n}i_{nq} + \omega_n i_{nd} \tag{8}$$

$$\frac{d}{dt}u_d = \frac{i_{nd}}{C_f} - \frac{i_{cd}}{Cf} - \omega_n u_q \tag{9}$$

$$\frac{d}{dt}u_q = \frac{i_{nq}}{C_f} - \frac{i_{cq}}{C_f} + \omega_n u_d \tag{10}$$

$$\frac{d}{dt}i_{cd} = \frac{u_d}{L_f} - \frac{v_d}{L_f} - \frac{R_f}{L_f}i_{cd} - \omega_n i_{cq} \tag{11}$$

$$\frac{d}{dt}i_{cq} = \frac{u_q}{L_f} - \frac{v_q}{L_f} - \frac{R_f}{L_f} + \omega_n i_{cd} \tag{12}$$

where i_{nd}, i_{nq}, i_{cd} and i_{cq} are the network and converter current d and q components, respectively; e_d, e_q, u_d, u_q, v_d and v_q are the network, point of common coupling (PCC) and converter voltage d and q components, respectively; L_n and L_f are the network and filter inductance, respectively; R_n and R_f are the network and filter resistances, respectively; C_f is the filter capacitance; and ω_n is the network frequency. The network impedance is varied in some simulations by altering the short-circuit ratio (SCR); this is discussed further in Section 3.1.

The DC link current is determined using the balance of power between the network and generator AC systems. The DC link voltage is then calculated using the current flowing into the DC link capacitor:

$$I_{DC} = \frac{P_n - P_g}{V_{DC}} \tag{13}$$

$$V_{DC} = \frac{I_{DC}}{sC_{DC}} \tag{14}$$

where V_{DC} is the DC link voltage, I_{DC} is the current flowing into the DC link capacitor, P_n and P_g are the network and generator power respectively and C_{DC} is the DC link capacitance.

2.2. Wind Turbine Control Structures

The control is split into the generator- and network-side converter controllers. A single generator control topology is used and three different network side controllers are presented: power voltage current control (PVCC), power voltage current control with inertia emulation (PVCCI) and a virtual synchronous machine. The DC link voltage control is tested on each converter separately for each control topology to allow for comparison.

The generator converter controller regulates the machine stator currents to alter the electromagnetic torque by varying the machine terminal voltages [26]. The inner loop is formed using two PI controllers with cross-coupling terms to account for the stator inductances:

$$V_{gq}^* = I_{gd}L_s\omega - K_{ig}(s)\left(I_{gq}^* - I_{gq}\right) \tag{15}$$

$$V_{gd}^* = I_{gq}L_s\omega - K_{ig}(s)\left(I_{gd}^* - I_{gd}\right) \tag{16}$$

$$K_{ig}(s) = \frac{k_{p,ig}s + k_{i,ig}}{s} \tag{17}$$

where $k_{p,ig}$ and $k_{i,ig}$ are the generator current controller proportional and integral gains, respectively. It is assumed that the exact generator rotational speed is known. The q-axis current command is augmented by an active damping algorithm for smoothing drivetrain oscillations and an inertia feedforward, K_{IFF}, to allow for the extraction of energy from the turbine during a frequency event when enabled (further discussed in Section 3.5). The active damping consists of a gain term, K_{dtd}, preceded by a bandpass filter. The filter centre frequency is tuned to the first eigenfrequency of the drivetrain [27]:

$$BPF(s) = \frac{2c\omega_{DT}s}{s^2 + 2c\omega_{DT}s + \omega_{DT}^2} \tag{18}$$

where c is the damping factor and ω_{DT} is the first eigenfrequency of the drivetrain. The feedforward term creates a frequency-based power command before converting to a current command and takes the form:

$$K_{IFF} = \frac{K_{FF}2K_{inert}}{3p\lambda\omega_m} \tag{19}$$

where K_{inert} is the inertia gain and K_{FF} is a gain parameter used to adjust the performance. The controller structure is shown in Figure 2.
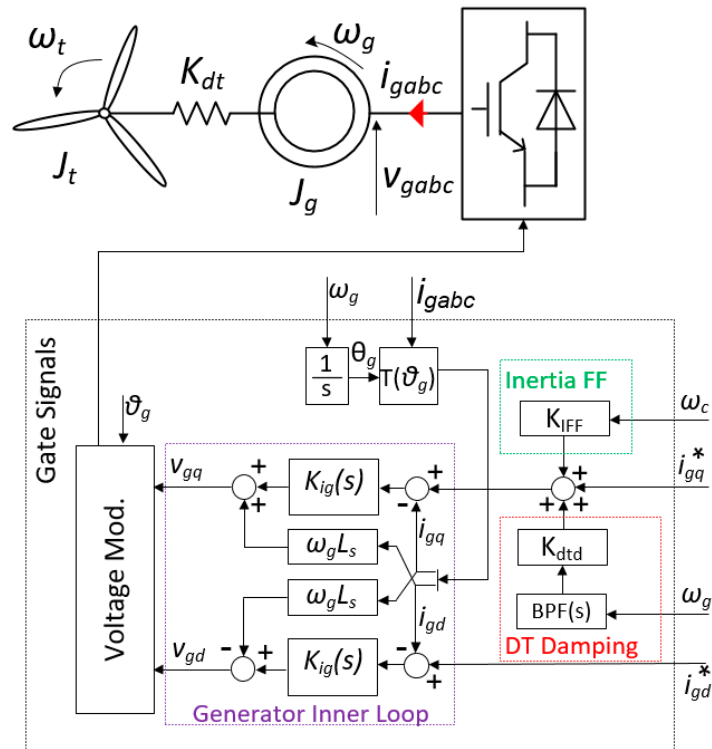

Figure 2. Generator controller structure. DT: Drivetrain, FF: Feedforward.

The network side inner loop current controller structure is similar to the generator side. However, on the network side, the PCC voltage is fed forward:

$$V_{cq}^* = U_q + I_{cd}L_f\omega - K_{ic}(s)\left(I_{cq}^* - I_{cq}\right) \tag{20}$$

$$V_{cd}^* = U_d - I_{cq}L_f\omega - K_{ic}(s)\left(I_{cd}^* - I_{cd}\right) \tag{21}$$

$$K_{ic}(s) = \frac{k_{p,in}s + k_{i,in}}{s} \tag{22}$$

where $k_{p,in}$ and $k_{i,in}$ are the network current controller proportional and integral gains, respectively. The controllers are tuned using the internal model control technique [28].

The standard outer loop controller is used to regulate the active power and voltage at the PCC. This is achieved by altering the references to the inner loop controller. The following control equations are aligned in the dq frame such that the q-axis controls the active power and the d-axis regulates the voltage at the PCC:

$$I_{cq}^* = K_{on,P}(s)(P_n^* - P_n) \tag{23}$$

$$I_{cd}^* = K_{on,U}(s)(U^* - U) \tag{24}$$

$$K_{oc,P}(s) = \frac{k_{p,onp}s + k_{i,onp}}{s} \tag{25}$$

$$K_{oc,U}(s) = \frac{-(k_{p,onu}s + k_{i,onu})}{s} \tag{26}$$

where $k_{p,onp}$ and $k_{i,onp}$ are the power loop proportional and integral gains, respectively, and $k_{p,onu}$ and $k_{i,onu}$ are the voltage loop proportional and integral gains, respectively. A phase-locked loop (PLL) is used to provide an estimation of the frequency using the following equation:

$$K_{PLL}(s) = \frac{k_{p,PLL}s + k_{i,PLL}}{s} \tag{27}$$

where $k_{p,PLL}$ and $k_{i,PLL}$ are the PLL proportional and integral gains, respectively. A schematic of the full controller, including the inner loop, is shown in Figure 3.
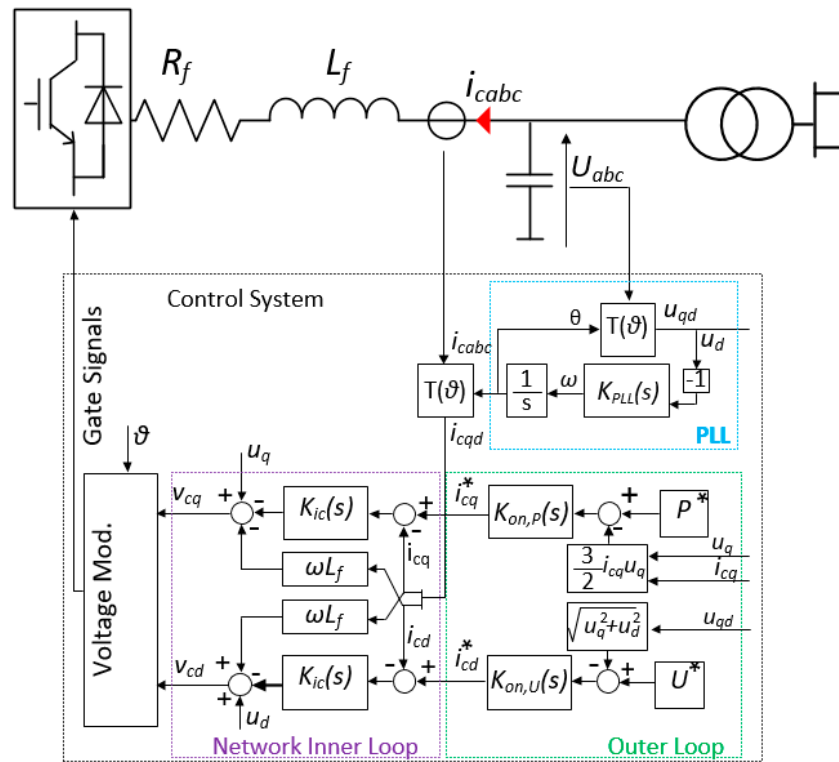
Figure 3. Power voltage current control (PVCC) controller diagram. PLL: Phase-Locked Loop.

The inertia emulation allows for the controller to respond to network frequency events. The inertia response is included by adding a component to the power command based on the rate of change of frequency (RoCoF). The governing equations are:

$$\Delta P_f = \omega_{PLL}K_{in}(s) \tag{28}$$

$$K_{in}(s) = K_{inert}\frac{Fk_d s}{s + F} \tag{29}$$

where K_{inert} is the inertial gain, ω_{PLL} is the estimation of the grid frequency provided by the PLL, F is the filter coefficient to smooth the derivative and k_d is the derivative gain. The control diagram of the PVCCI controller is shown in Figure 4.
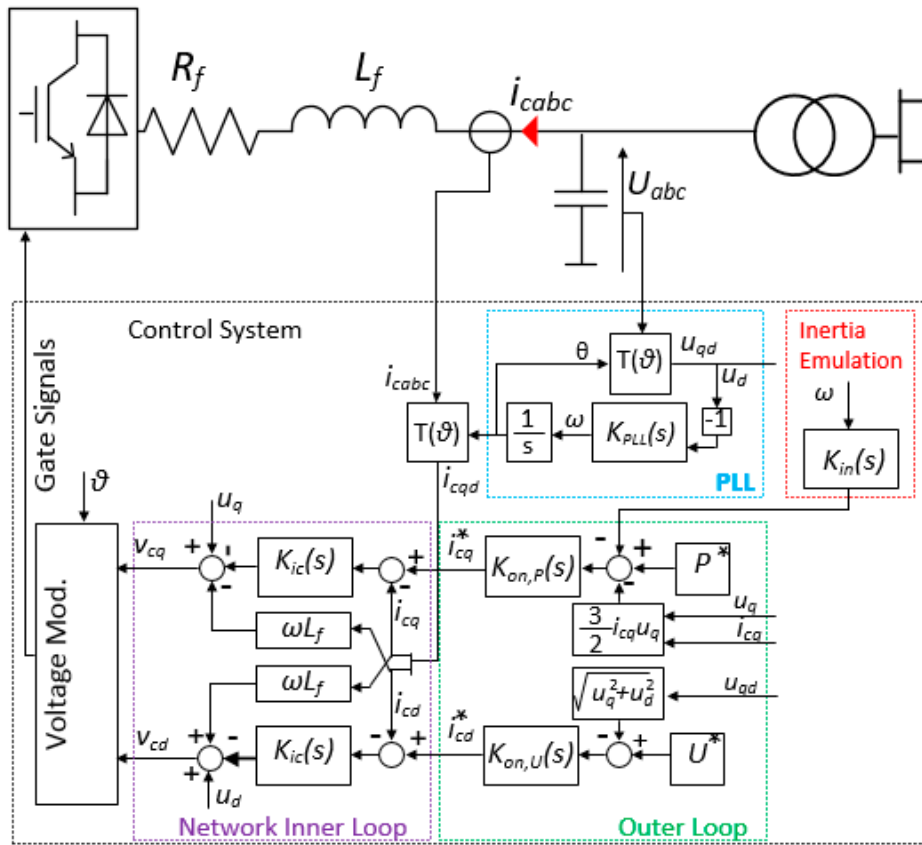
Figure 4. Power voltage current control with inertia emulation controller diagram.

The VSM controller is a grid-forming algorithm that does not rely on a PLL estimation of the grid frequency. The Park transformations become Clarke transformations as the angle input is zero. The converter voltage angle is generated via an active power controller, inspired by the synchronous machine equations, and the voltage magnitude is provided by a voltage controller that regulates the voltage at the PCC. Therefore, the inner loop current control is no longer present. The following control equations are implemented:

$$\theta_c = \frac{K_{VSM}(s)(P_n^* - P_n)}{s} \tag{30}$$

$$V_{cq}^* = K_v(s)(U^* - U) \tag{31}$$

$$K_{VSM}(s) = \frac{k_{p,VSM}s + k_{i,VSM}}{s} \tag{32}$$

$$K_v(s) = \frac{k_{p,v}s + k_{i,v}}{s} \tag{33}$$

where θ_c is the converter angle given by the VSM algorithm; $K_{p,VSM}$ and $K_{i,VSM}$ are the VSM power controller proportional and integral gains, respectively; and $K_{p,v}$ and $K_{i,v}$ are the voltage controller proportional and integral gains, respectively. A control diagram is shown in Figure 5.
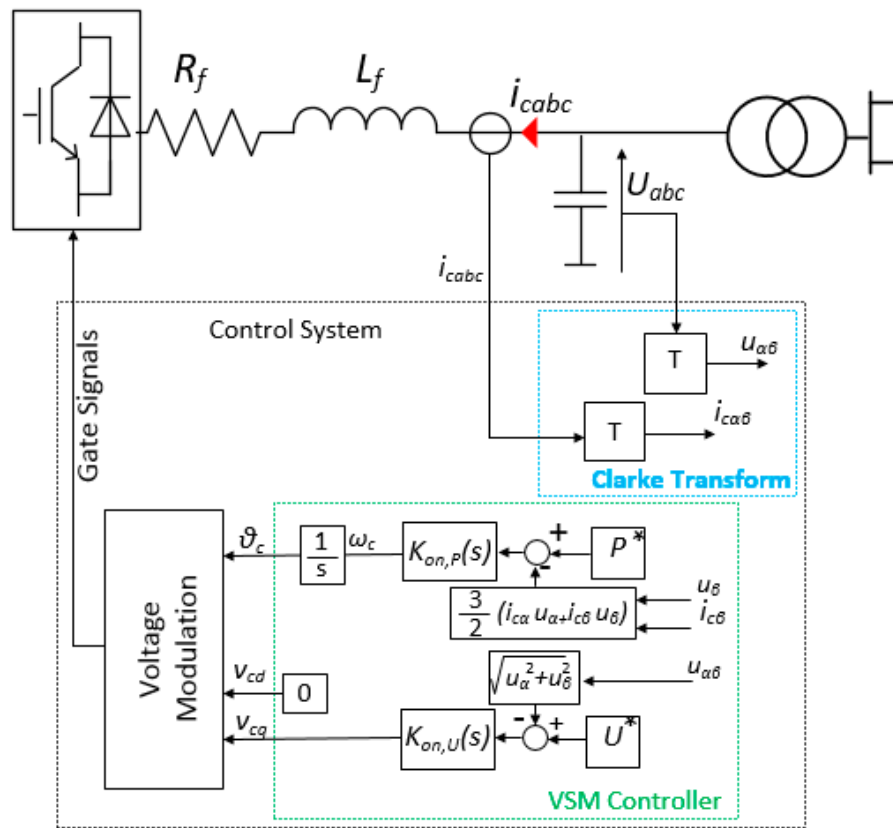
Figure 5. Virtual synchronous machine (VSM) controller diagram.

The outer-loop controller for each structure was designed to regulate the active power and voltage at the PCC. For this study, only a single wind turbine was considered. However, if a larger network was to be considered, the outer-loop setpoints for each unit would be given via another secondary control structure, optimising the output of the farm along with other distributed resources. A number of methods exist for this focussing on the wind farm itself [29], or by considering the wind park as a distributed energy resource (DER) within a microgrid [30]. However, further considerations on this are out with the scope of this paper.

When the DC link voltage is regulated by the network converter, the active power command for the outer loop controller is provided by a PI controller acting on the DC link voltage error. This connection is shown by the dotted line in Figure 1. The following equations governs the control:

$$P_n^* = K_{VDC_n}\left(V_{DC}^* - V_{DC}\right) \tag{34}$$

$$K_{VDC_n} = \frac{k_{p-VDC}s + k_{i-VDC}}{s} \tag{35}$$

where k_{p-VDC} and k_{i-VDC} are the DC link voltage controller proportional and integral gains, respectively.

When the DC link is placed in the generator side converter controller, the same governing Equations (23) and (24) are used. However, in this case, the output of the controller is the generator q-axis current command. Due to this, the controller gains are considerably smaller. This connection is shown in Figure 1 by the dashed line. Note that the DC link voltage control is only active on one converter at any given time.

2.3. Small-Signal Modelling

The small-signal model approximates the behaviour of the system using linear equations, which allows for analysis using standard control analysis tools. The system contains non-linear

components that must be linearised around the operating point of interest and must be reconsidered if the operating point is moved. The linearised system containing the PLL based controllers is shown in Figure 6 and the VSM system is shown in Figure 7. Note that only the systems requiring linearisation are discussed; the matrices for the other components are constructed from the equations mentioned in Sections 2.1 and 2.2.
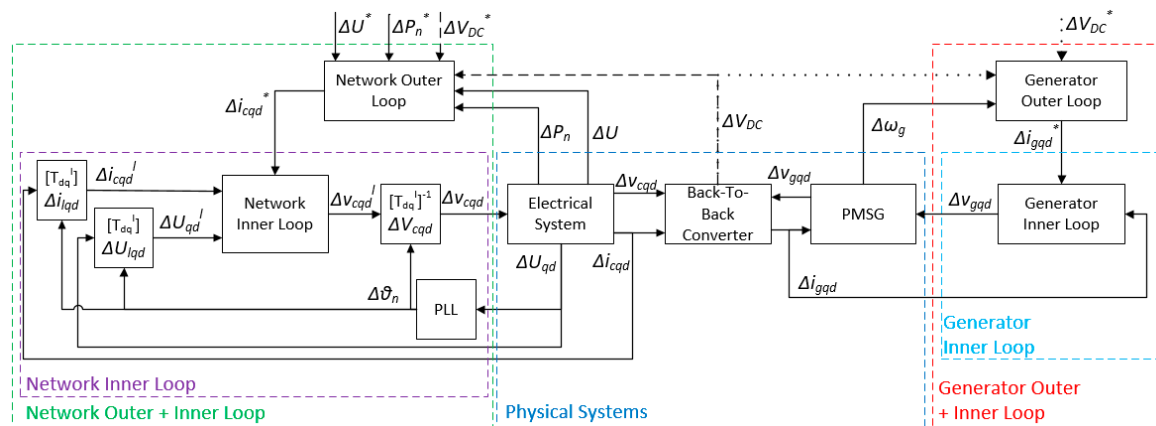

Figure 6. Linearised system for PLL-based controllers. PMSG: Permanent Magnet Synchronous Generator.
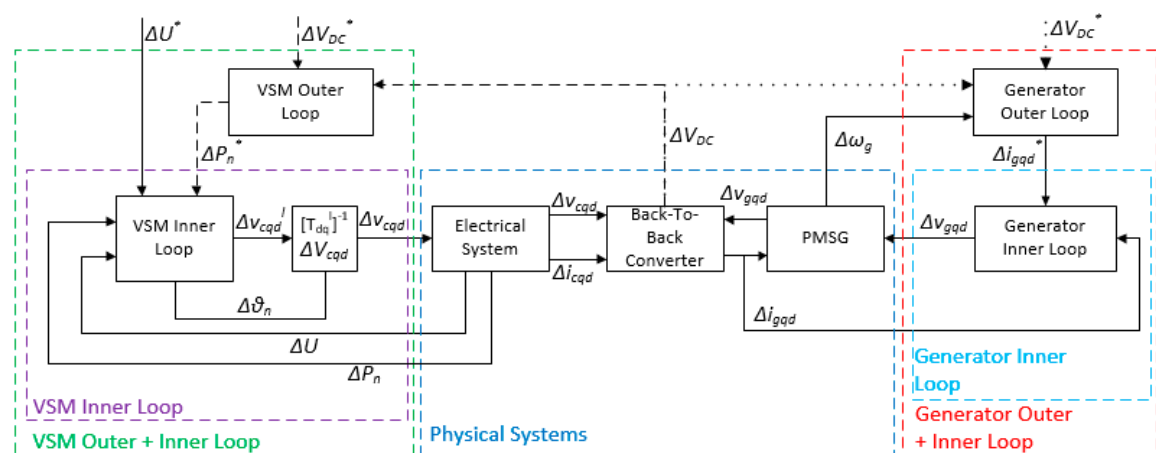
Figure 7. Linearised system for VSM controllers.

The PLL is used to provide an estimation of the network frequency to the park and inverse park transforms. Since the feedback of the PLL involves the park transform, the system is non-linear. In the linearised model, the PLL introduces an angle deviation when the system is moved from the original operating point [31]. The PLL was linearised following Zhang [32] and the following equation was produced:

$$\Delta\theta = \frac{k_{p-pll}s + k_{i-pll}}{s^2 + U_{q0}k_{p-pll}s + U_{q0}k_{i-pll}}\Delta U_d \tag{36}$$

Even though the system is modelled in the dq frame, the park and inverse park transforms must still be accounted for. Note that this is only necessary for the network side; the generator side converter has an exact measure of the generator frequency and therefore the transforms introduce no deviation and can be disregarded. Since the transformations are non-linear, they must be linearised before being added to the small-signal model. The l superscript denotes variables that have been transformed using the linearised transformations. The linearised park transform is expressed as:

$$x_{dq}^l = \left[T_{dq}^l\right]\left[\Delta x_d \ \Delta x_q \ \Delta\theta\right] \tag{37}$$

$$\left[T_{dq}^l\right] = \begin{bmatrix} \cos(\theta_0) & -\sin(\theta_0) & -\sin(\theta_0)x_{d0} - \cos(\theta_0)x_{q0} \\ \sin(\theta_0) & \cos(\theta_0) & \cos(\theta_0)x_{d0} - \sin(\theta_0)x_{q0} \end{bmatrix} \tag{38}$$

The linearised inverse transform is given as:

$$x_{dq} = \left[T_{dq}^l\right]^{-1}\left[\Delta x_d^l \ \Delta x_q^l \ \Delta\theta\right]^T \tag{39}$$

$$\left[T_{dq}^l\right]^{-1} = \begin{bmatrix} \cos(\theta_0) & \sin(\theta_0) & \cos(\theta_0)x_{d0} - \sin(\theta_0)x_{q0} \\ -\sin(\theta_0) & \cos(\theta_0) & -\cos(\theta_0)x_{d0} - \sin(\theta_0)x_{q0} \end{bmatrix} \tag{40}$$

where θ_0, x_{d0} and x_{q0} are the initial values of the network angle, d-component and q-component, respectively, based on the linearisation point.

Normally, the electrical system is linearised to provide the active power and voltage magnitude at the PCC. However, the linearised power and voltage requires the park-transformed variables. Therefore, the quantities are calculated within the grid controller and the electrical system needs no linearisation. The inner loop is constructed using the following state-space representation:

$$\Delta\dot{x}_i^l = B_i^l\Delta u_i^l \tag{41}$$

$$\Delta y_i^l = C_i^l\Delta x_i^l + D_i^l\Delta u_i^l \tag{42}$$

where the state variables, input and output are:

$$\Delta x_i^l = \begin{bmatrix} \Delta ei_{cq}^l & \Delta ei_{cd}^l \end{bmatrix} \tag{43}$$

$$\Delta u_i^l = \begin{bmatrix} \Delta i_{cq}^* & \Delta i_{cd}^* & \Delta i_{cq}^l & \Delta i_{cd}^l & \Delta U_q^l & \Delta U_d^l \end{bmatrix} \tag{44}$$

$$\Delta u_i^l = \begin{bmatrix} \Delta i_{cq}^* & \Delta i_{cd}^* & \Delta i_{cq}^l & \Delta i_{cd}^l & \Delta U_q^l & \Delta U_d^l \end{bmatrix} \tag{45}$$

where Δei_{qd}^l are the current errors given by the difference between Δi_{qd}^* and Δi_{qd}^l. The state space matrices are:

$$B_i^l = \begin{bmatrix} -1 & 0 & 1 & 0 & 0 & 0 \\ 0 & -1 & 0 & 1 & 0 & 0 \end{bmatrix} \tag{46}$$

$$C_i^l = \begin{bmatrix} k_{i,in} & 0 \\ 0 & k_{i,in} \\ 0 & 0 \\ 0 & 0 \end{bmatrix} \tag{47}$$

$$D_i^l = \begin{bmatrix} -k_{p,in} & 0 & k_{p,in} & -\omega_n L_f & 1 & 0 \\ 0 & -k_{p,in} & \omega_n L_f & k_{p,in} & 0 & 1 \\ 0 & 0 & \frac{3U_{q0}}{2} & \frac{3U_{d0}}{2} & \frac{3I_{q0}}{2} & \frac{3I_{d0}}{2} \\ 0 & 0 & 0 & 0 & \frac{U_{q0}}{U_{m0}} & \frac{U_{d0}}{U_{m0}} \end{bmatrix} \tag{48}$$

where U_{q0}, U_{d0}, I_{q0}, I_{d0} and U_{m0} are the initial values of the PCC voltage q and d components, converter current q and d components and the PCC voltage magnitude, respectively, based on the linearisation point.

The DC link is one part of the electrical system that does require linearisation to accurately calculate the DC link voltage. The state space matrices are constructed as follows:

$$A_{DC} = \begin{bmatrix} \dfrac{P_{g0} - P_{n0}}{C_{DC}V_{DC0}^2} \end{bmatrix} \tag{49}$$

$$B_{DC} = \begin{bmatrix} -\dfrac{1}{C_{DC}V_{DC0}} & \dfrac{1}{C_{DC}V_{DC0}} \end{bmatrix} \tag{50}$$

$$C_{DC} = [1] \tag{51}$$

$$D_{DC} = [0] \tag{52}$$

where P_{g0}, P_{n0} and V_{DC0} are the initial values of the generator power, network power and DC link voltage based on the operating point, and C_{DC} is the DC link capacitance.

Finally, filters are used in the stationary abc reference frame to model the bandwidth of the measurement devices. These are applied to the PCC voltage U and converter current i_{cabc}. The filters are transformed into the synchronous reference frame to give the following matrices, where D_f is a 2×2 matrix of zeros:

$$A_f = \begin{bmatrix} -\frac{1}{T_f} & -\omega_n \\ \omega_n & -\frac{1}{T_f} \end{bmatrix} \tag{53}$$

$$B_f = \begin{bmatrix} \frac{1}{T_f} & 0 \\ 0 & \frac{1}{T_f} \end{bmatrix} \tag{54}$$

$$C_f = \begin{bmatrix} 1 & 0 \\ 0 & 1 \end{bmatrix} \tag{55}$$

where ω_n is the base network frequency and T_f is the filter time constant.

3. System Analysis

This section first presents a verification of the constructed models. It then analyses the performance of the different grid-side converter controllers by considering the connection to a stiff DC link voltage modelled as a battery. This allows for the decoupling of the generator and drivetrain dynamics to ensure proper operation of the network controllers. The effect of differing network impedances is also investigated using the battery-connected models. Following this, the variations between applying the DC link voltage controller to the generator- or network-side converter is investigated, including all dynamics from the drivetrain to the network. Further study is then completed on the generator- and network-side converters by analysing the effect of different controller gains on the ability of the converter to respond to external events. The parameters for all analyses are shown in Table 1. The parameters used are given for standard operating conditions and are assumed to remain constant during all tests. The only components dependent on environmental operating conditions are the impedances. These are very small and do not vary greatly with changing conditions.

3.1. Small-Signal Model Validation

The small-signal models were compared against a verified time domain model to ensure each part of the system was responding correctly to power and frequency steps within allowable errors.

3.1.1. Battery-Connected Models

First, the battery-connected models were checked to ensure the network-side converter was responding correctly to power and frequency steps. This allowed the models to be used as a baseline for comparison as further system components were added to increase the complexity. The output of the battery-connected models can be viewed in Figure 8 with the percentage error between the small-signal and detailed models shown in Figure 9. A 100-W step in power was applied at 3 s (a,c,e) and a 0.2 rads^{-1} step was applied at 5 s (b,d,f). The validation data is provided as supplementary material at the doi given in the Supplementary Materials section.

Table 1. Parameter values.

Parameter	Value	Parameter	Value
E	690 V	$k_{i,ig}$	5
C_f	34.1 μF	$k_{p,in}$	0.0253
L_f	50.5 μH	$k_{i,in}$	0.7935
R_f	1.6 mΩ	$k_{p,onp}$	0.0029
C_{DC}	11.2 mF	$k_{i,onp}$	1
R_s	2.7 mΩ	$k_{p,onu}$	20
L_s	0.526 mH	$k_{i,onu}$	1000
J_t	12,892,100 kgm^2	K_{inert}	100,000
J_g	1,371,500 kgm^2	F	100
K_{DT}	21,264,367 Nm^{-1}	K_d	0.1
ω_{DT}	4.14 rads^{-1}	$k_{p,VSM}$	8×10^{-7}
c	1	$k_{i.VSM}$	2×10^{-5}
p	80	$k_{p,v}$	0.02
ω_m	1.885 rads^{-1}	$k_{i,v}$	50
T_f	0.1 ms	k_{p-pll}	0.7885
$k_{p,ig}$	2	k_{i-pll}	175.1847

All analyses were conducted use a converter rating of 3 MW.
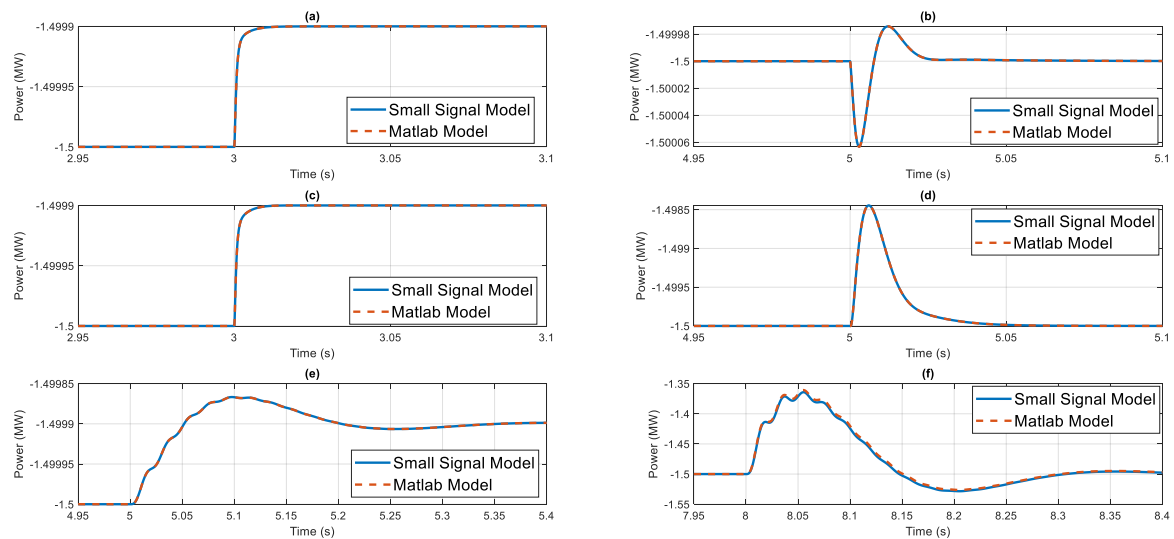
Figure 8. Validation of the battery-connected small-signal models: (**a**) net power command step (100 W) to net power for PVCC, (**b**) net frequency step (0.2 rad/s) to net power for PVCC, (**c**) net power command step (100 W) to net power for PVCC with inertia emulation (PVCCI), (**d**) net frequency step (0.2 rad/s) to net power for PVCCI, (**e**) net power command step (100 W) to net power for VSM and (**f**) net frequency step (0.2 rad/s) to net power for VSM.
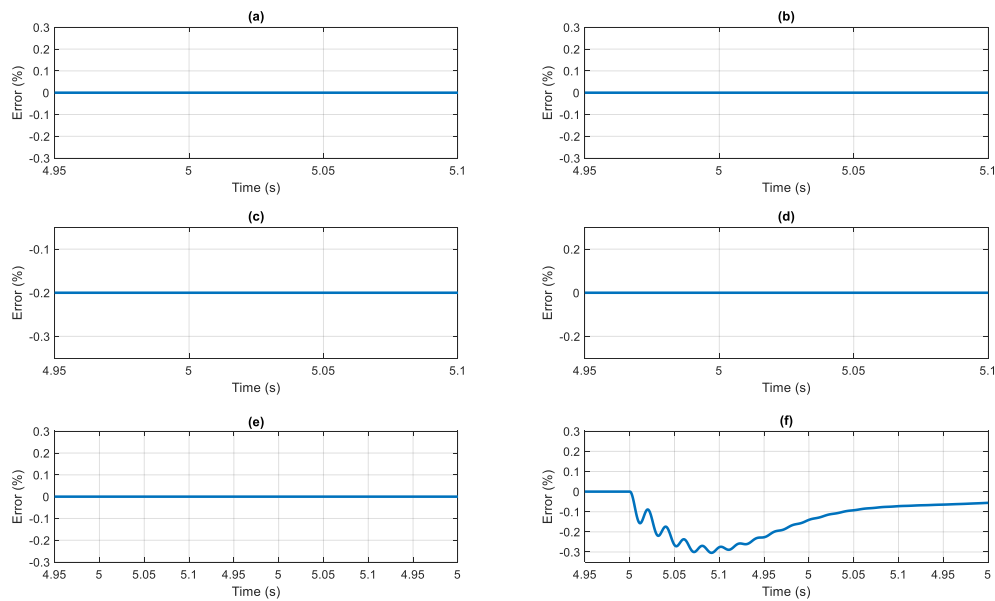
Figure 9. Validation of battery connected small-signal models: (**a**) net power command step (100 W) to net power error for PVCC, (**b**) net frequency step (0.2 rad/s) to net power error for PVCC, (**c**) net power command step (100 W) to net power error for PVCCI, (**d**) net frequency step (0.2 rad/s) to net power error for PVCCI, (**e**) net power command step (100 W) to net power error for VSM and (**f**) net frequency step (0.2 rad/s) to net power error for VSM.

Figure 8 shows a good match between the small-signal and time-domain models for all three controllers undergoing both a power and frequency step. The traces for the PVCC (a,b) and PVCCI (c,d) overlay almost exactly, which is further observed in Figure 9 The absolute percentage error for both the PVCC and PVCCI during a power step was less than 5×10^{-7}% (a,c) and below 2×10^{-5} % (b,d) for a frequency step. The absolute error for a power step when operating in VSM was also very small (1×10^{-6}%) (e); however, for a frequency step, the error was larger with a maximum of 0.3% (f). All errors indicated a close match for the battery-connected models.

3.1.2. Full Wind Turbine Models

The full models, including the network, generator, DC link and drivetrain, along with the network- and generator-side controllers, are compared in this section. The DC link voltage control is validated as part of both the network (DC Net)- and generator (DC Gen)-side controllers. The output can be viewed in Figure 10, with the percentage error between the two model types shown in Figure 11. The power response was given by a 1 A step in the generator q-axis current command (a,c,e,g) and the frequency response by a (0.2 rads^{-1}) network frequency step (b,d,f,h).
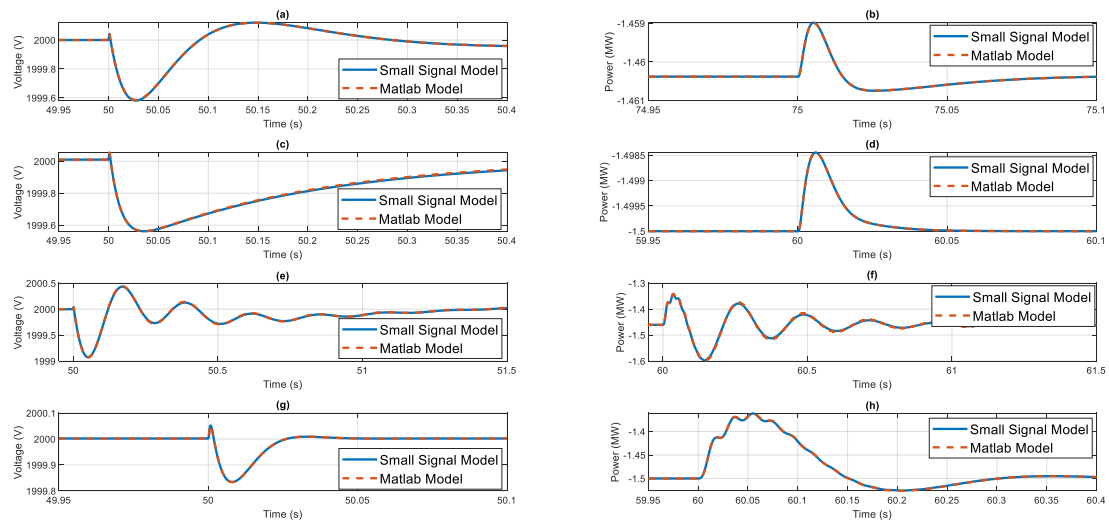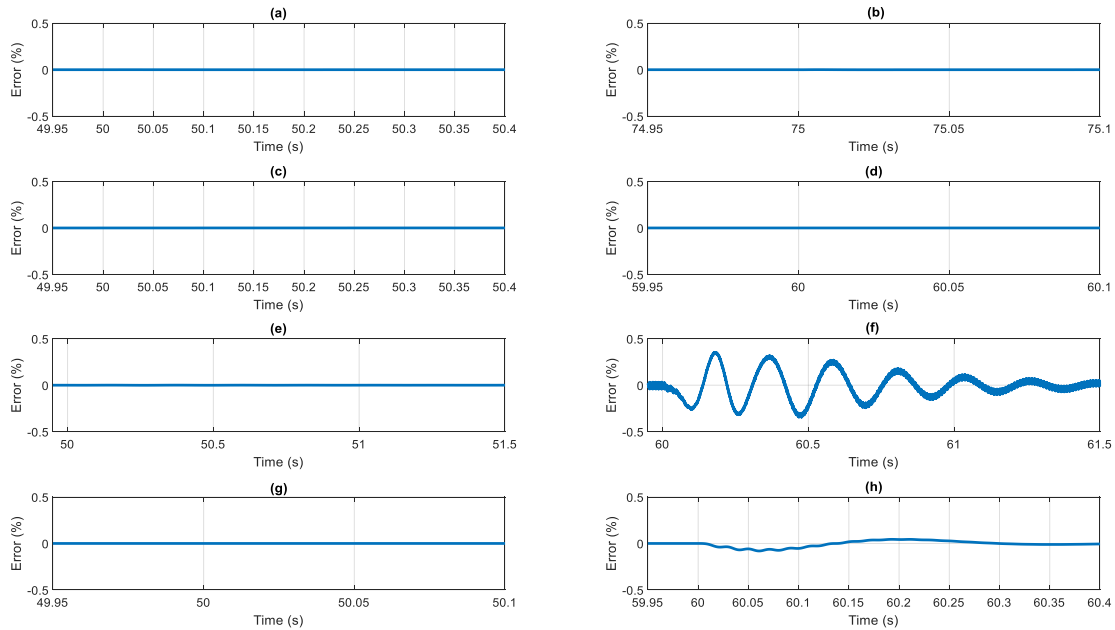
Figure 10. Validation of the drivetrain small-signal models: (**a**) Gen q-axis current step (1 A) to network power—PVCCI DC Net, (**b**) Net frequency step (0.2 rad/s) to network power—PVCCI DC Net, (**c**) Gen q-axis current step (1 A) to network power—PVCCI DC Gen, (**d**) Net frequency step (0.2 rad/s) to network power—PVCCI DC Gen, (**e**) Gen q-axis current step (1 A) to network power—VSM DC Net, (**f**) Net frequency step (0.2 rad/s) to network power—VSM DC Net, (**g**) Gen q-axis current step (1 A) to network power—VSM DC Gen and (**h**) Net frequency step (0.2 rad/s) to network power—VSM DC Gen.

Figure 11. Validation of the drivetrain connected small-signal models: (**a**) Gen q-axis current step (1 A) to network power error for PVCCI DC Net, (**b**) Net frequency step (0.2 rad/s) to network power error for PVCCI DC Net, (**c**) Gen q-axis current step (1 A) to network power error for PVCCI DC Gen, (**d**) Net frequency step (0.2 rad/s) to network power error for PVCCI DC Gen, (**e**) Gen q-axis current step (1 A) to network power error for VSM DC Net, (**f**) Net frequency step (0.2 rad/s) to network power error for VSM DC Net, (**g**) Gen q-axis current step (1 A) to network power error for VSM DC Gen and (**h**) Net frequency step (0.2 rad/s) to network power error for VSM DC Gen.

From Figure 10, a good match can be observed for all four configurations for both a power and frequency step. Looking at Figure 11, the power response shown in the left-side plots exhibited very small errors ($< 1 \times 10^{-3}$%) (a,c,e,g). The error for the PVCCI undergoing a frequency step was marginally

higher for the network side DC link voltage control (b) over the generator side (d). As observed with the battery connected cases, the VSM error was higher when a frequency step occurred, with the network side DC link voltage (f) control again being slightly larger. The maximum error of 0.4% was well within the acceptable range.

3.2. Small-Signal Analysis of the Different Network Side Converter Controllers

Following verification, the operation of each controller in response to frequency events was analysed. The three control topologies responded differently in the low-frequency inertial range. This study focussed on the behaviour of the network side converter operating under the three control schemes for different grid impedances. Therefore, the ideal case was used where the DC link was modelled as a battery to easily compare the controller performance while ignoring external factors. The controller topologies are compared in Bode plots shown in Figure 12.
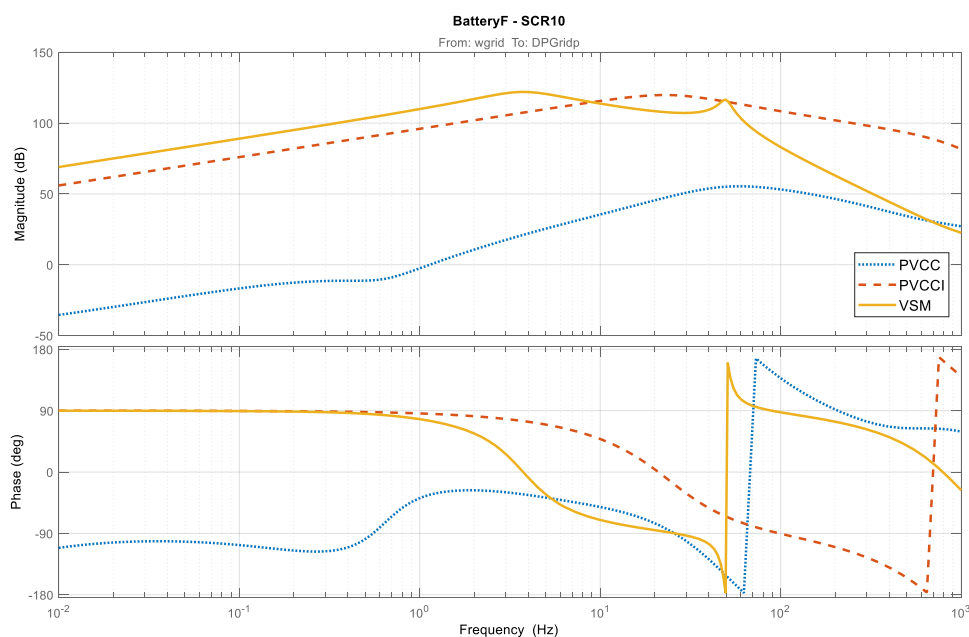
Figure 12. Bode plots comparing the frequency response of each control topology.

Looking at Figure 12, the important differences to be noted occur in the frequency range of 1–10 Hz. The gain at these frequencies dictate the inertial performance of the controller [6]. If the dotted blue trace is examined, the PVCC controller had the lowest gain response around the inertial frequencies, indicating a poor response. The dashed orange trace illustrates the effect when the inertia emulation is added; the gain response in the low-frequency region was increased, representing an improved inertia delivery during a frequency event. The VSM controller, shown in solid yellow, exhibited the best inertial response, giving the highest gain response in the low-frequency range with a shallow peak at approximately 3.5 Hz. This peak could be sharpened and the frequency at which it occurred was dependent on the tuning of the proportional and integral gains within the controller. The plot shown in Figure 12 was when the system SCR was 10. Varying the SCR can affect the performance of the controllers; to investigate this, the power and frequency response of the three controllers were compared for three different SCRs: 2, 3 and 10. The closed loop responses of the network power command to network power are shown in Figure 13 and the frequency responses from network frequency to network power are shown in Figure 14.
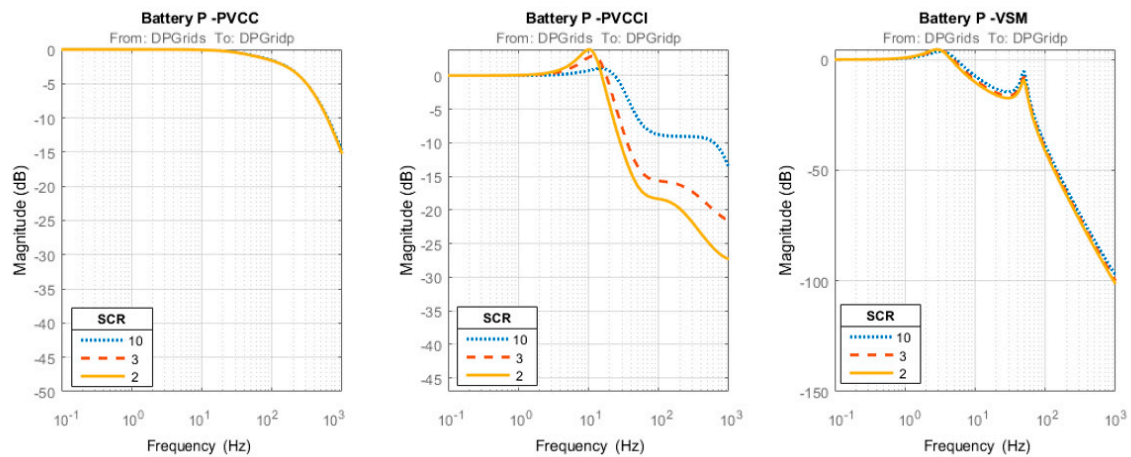
Figure 13. Power responses for the battery-connected controllers for different (SCRs).

Looking at Figure 13, the SCR had little effect on the PVCC below 1000 Hz. The PVCCI gain response began to deviate much faster with a small peak forming around 10 Hz for an SCR of 2. As the SCR reduced, this peak began to flatten, while the frequency at which the highest point occurred increased. After this, both the gain and frequency responses deviated greatly. The gain response decayed faster for a lower short-circuit ratio. The SCR had the least effect on the VSM controller. As the SCR increased, the peak of the inertial response rose, while the frequency at which the peak occurred also increased. Overall, the decay rate in the magnitude response beyond 10 Hz was the largest for the VSM, followed by the PVCCI and finally the PVCC.
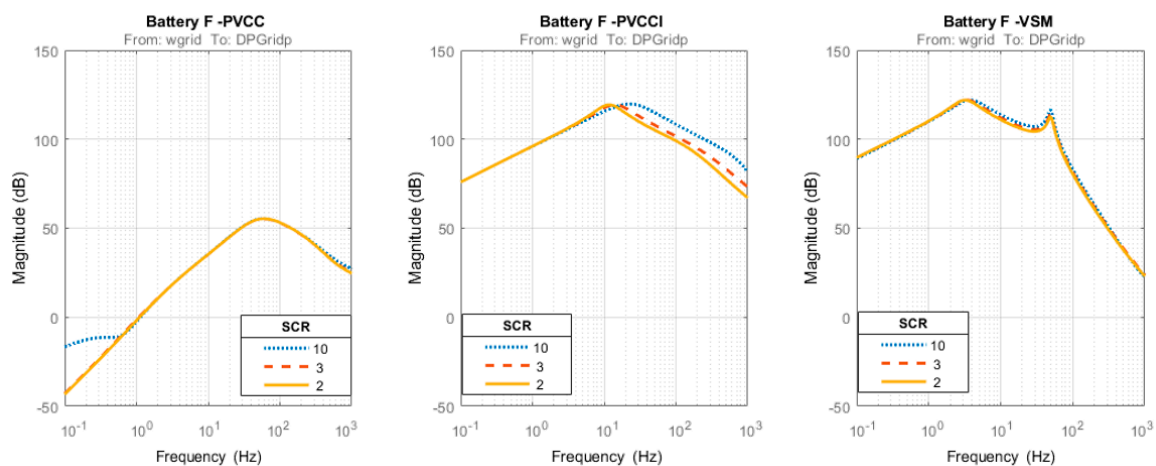
Figure 14. Frequency responses for the battery-connected controllers for different SCRs.

From Figure 14, the PVCC performance was largely unaffected by the varying SCR in the range of 1–1000 Hz. A small deviation can be seen beyond 1000 Hz. The responses of the PVCCI varied little for 1–8 Hz; beyond 8 Hz, the decay rate increased with a decreasing SCR. A sharper peak was formed when an SCR of 2 was used, with the frequency response beginning to match closer with the VSM traces. Similar to Figure 13, the SCR had little effect on the operation of the VSM controller in Figure 14. The peak occurring at 50 Hz was slightly higher for the highest SCR. The inertial response remained largely the same with the location of the peak response increasing in frequency slightly as the SCR increased.

3.3. DC Link Voltage Control Location Comparison

The control of the DC link voltage can be part of the generator- or network-side converter control. Each topology has advantages and disadvantages, as discussed in Sections 3.4 and 3.5. A key feature

of the comparison is the inertial response of the network converter. The frequency response under a step of 1 rads^{-1} was analysed for both locations, along with the battery-connected system for reference. The effect of the DC link voltage control location on the frequency response can be seen in the Bode plots presented in Figure 15 for the VSM controller. The difference in the response to the frequency step for each system is shown in Figure 16.
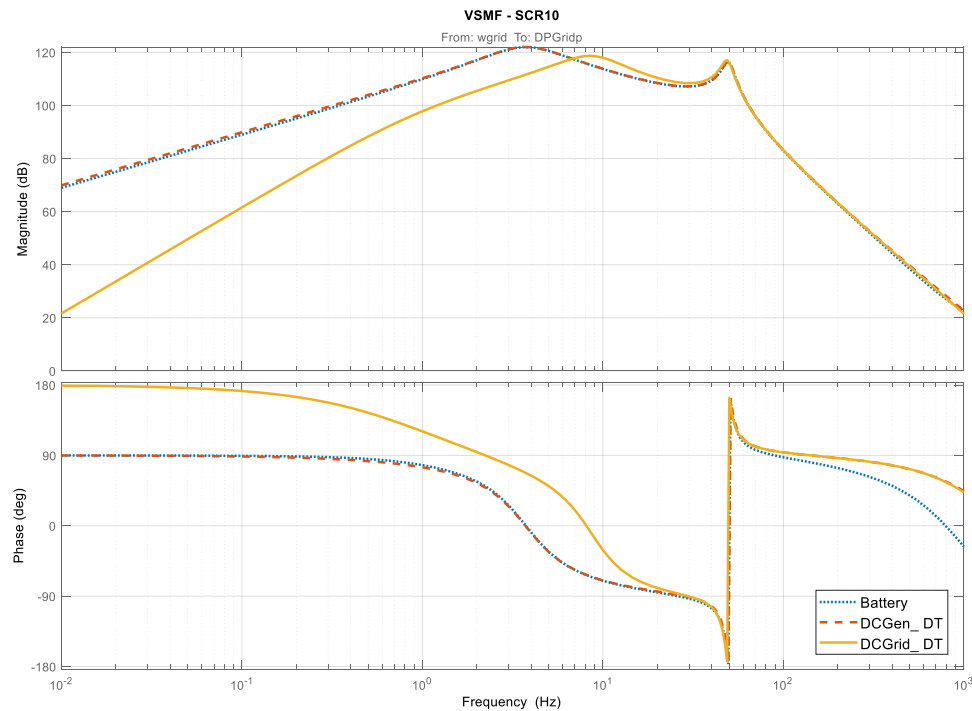
Figure 15. Bode plots comparing frequency responses for DC link voltage control location for VSM controller.
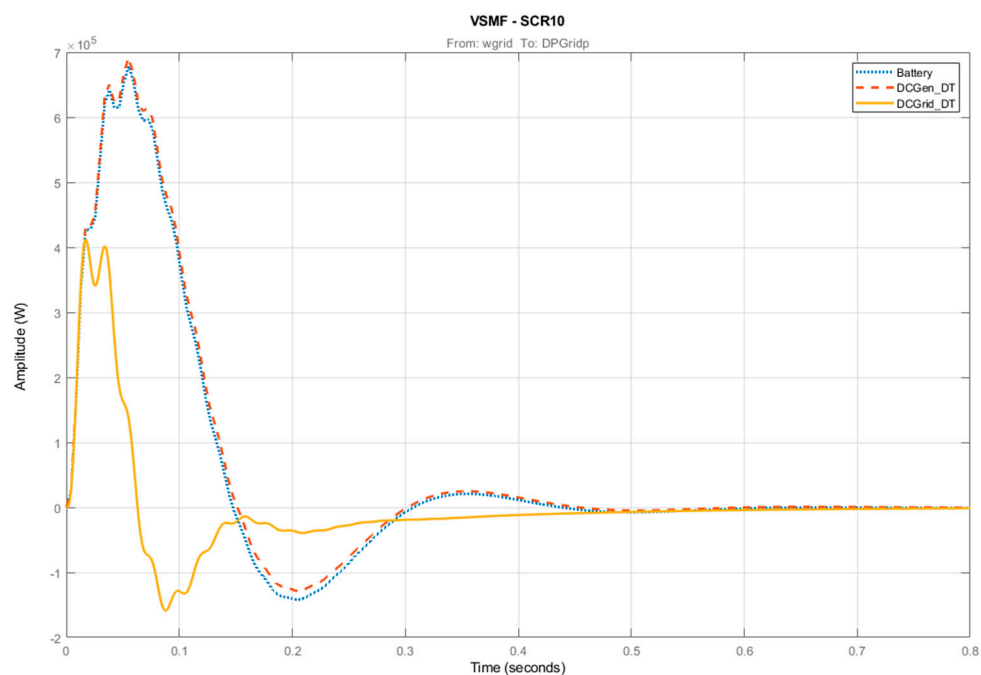
Figure 16. Step response comparing the DC link voltage control location frequency responses.

Looking at Figure 15, each of the three topologies had different gain and phase responses. The battery-connected system, shown in dotted blue, exhibited a similar response to the system with the DC link voltage control on the generator side, shown in dashed orange. This was expected, as long as the DC link voltage controller was fast enough to prevent the DC link voltage falling significantly during power changes. The gain response was around 10% smaller throughout the low-frequency range of interest.

From Figure 16, all three systems remained stable under a frequency step. Active power was increased quickly, representing an absorption by the network converter. More active power was absorbed by the battery-connected and generator-side DC link control systems, which agrees with Figure 15. There was a reduction of around 250 kW when the DC link control was moved to the network side for the given frequency step.

3.4. Generator-Side Converter DC Link Voltage Control

When the DC link voltage was regulated via the generator-side converter, a different reaction occurred within the control. In this case, the DC link voltage loop appeared to oppose the active damping of the torsional drivetrain vibrations. The problem was exacerbated when the DC link voltage gains were increased to reduce the settling time from disturbances. Figure 17 illustrates this effect with a step response to a 1 rads^{-1} step in network frequency. Figure 18 shows the Bode plots of the system from the input of the network frequency to the outputs of generator mechanical speed and DC link voltage, respectively.
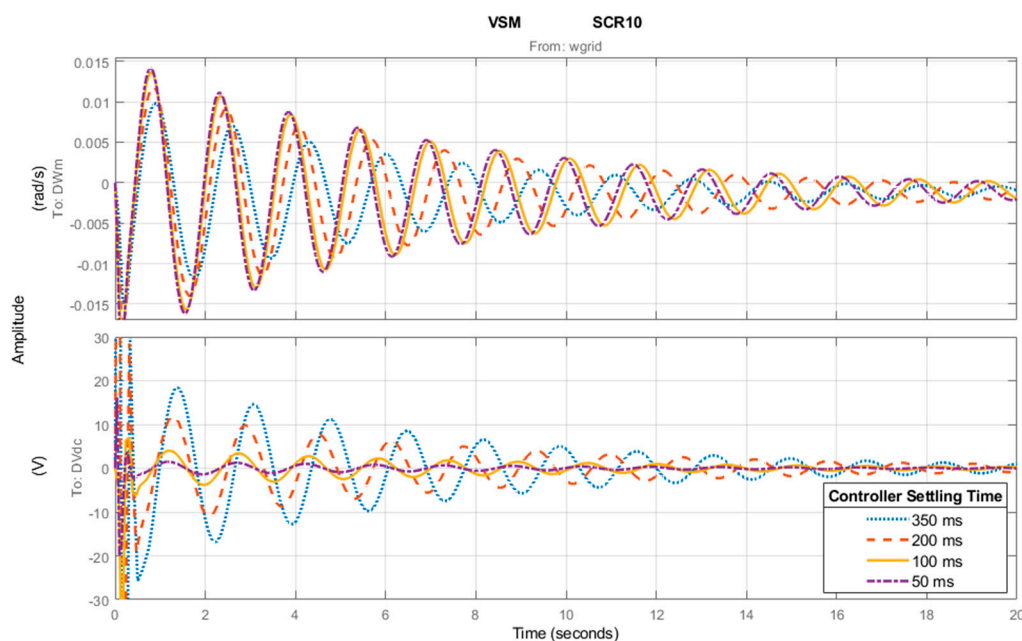

Figure 17. Step response comparing the generator-side DC link voltage controller tunings.
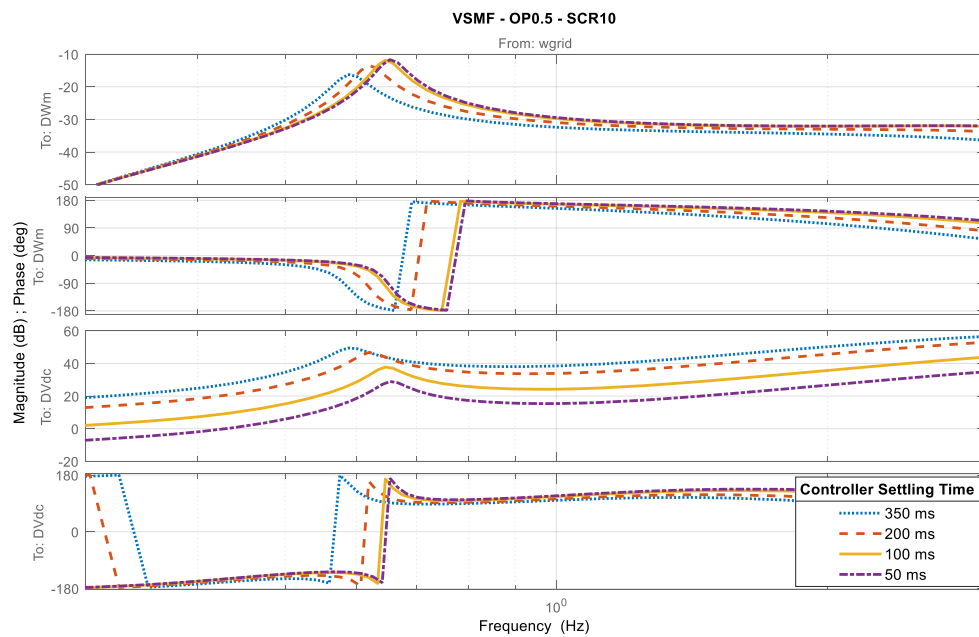
Figure 18. Bode plots comparing the generator-side DC link voltage controller tunings.

Looking at Figure 17 the oscillations in the mechanical speed (upper plot) were smaller, decayed faster and were of lower frequency as the DC link voltage controller speed was reduced. This indicates that the active damping was better at slow controller tunings. If the lower plot in Figure 17 is considered, the DC link voltage experienced larger fluctuations when the DC link voltage controller was tuned slowly (blue dotted line). This suggests a trade-off between drivetrain damping and DC link voltage disturbance rejection when the control of the DC link is governed by the generator-side converter. This idea is further solidified in Figure 18; by considering the mechanical speed in the upper plot, the peak was the lowest for the slowest DC link controller tuning and largest for the fastest tuning, confirming the improved damping for slower DC link tunings. However, when the lower plot in Figure 18 is studied, the magnitude response peak was much greater when the DC link controller was tuned slowly, further indicating a large upset in the DC voltage when the controller gains were slow.

3.5. Network-Side DC Link Voltage Control

When the responsibility for controlling the DC link voltage is left to the network-side converter, the power command is altered when the DC link voltage deviates. Since the DC link voltage varies as the network power changes, as is the case during frequency events for the VSM controller and PVCCI, it is clear there will be an interaction between the DC link voltage control and the inertial response. To investigate this, both the VSM controller and PVCCI were subjected to a frequency step of +0.2 rads^{-1} and the DC link voltage controller gains were varied. Figure 19 presents a Bode plot illustrating the effect when the DC link controller proportional and integral gains were increased to alter the controller bandwidth. Figure 20 shows the network converter step response.
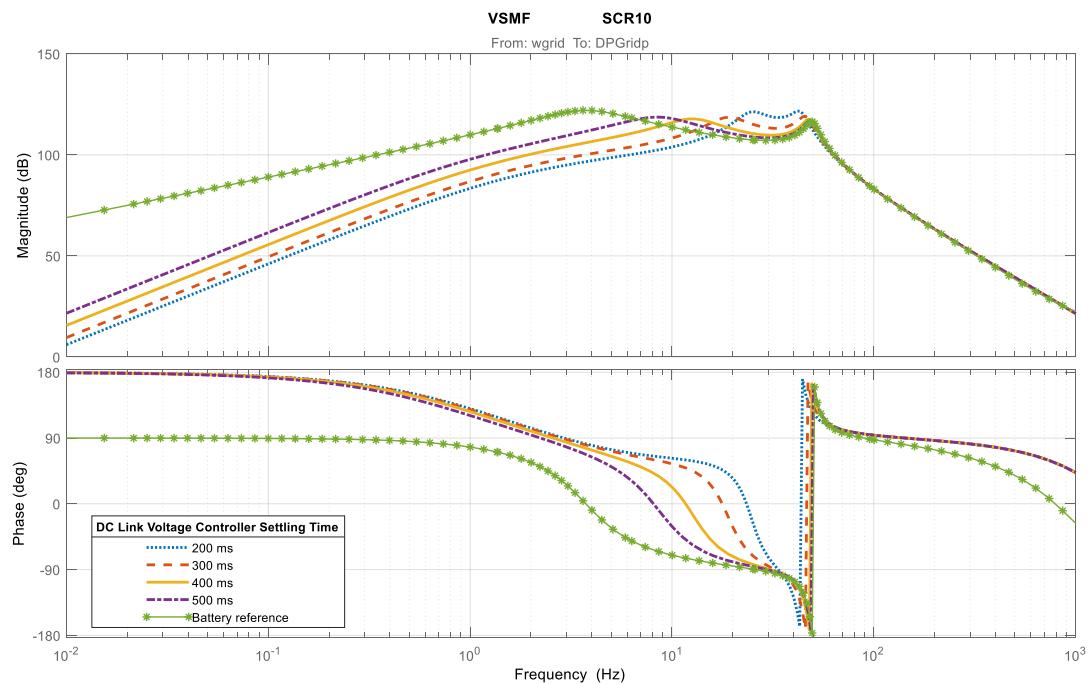
Figure 19. Bode plots showing the effect of the DC link controller bandwidth on the VSM frequency response.
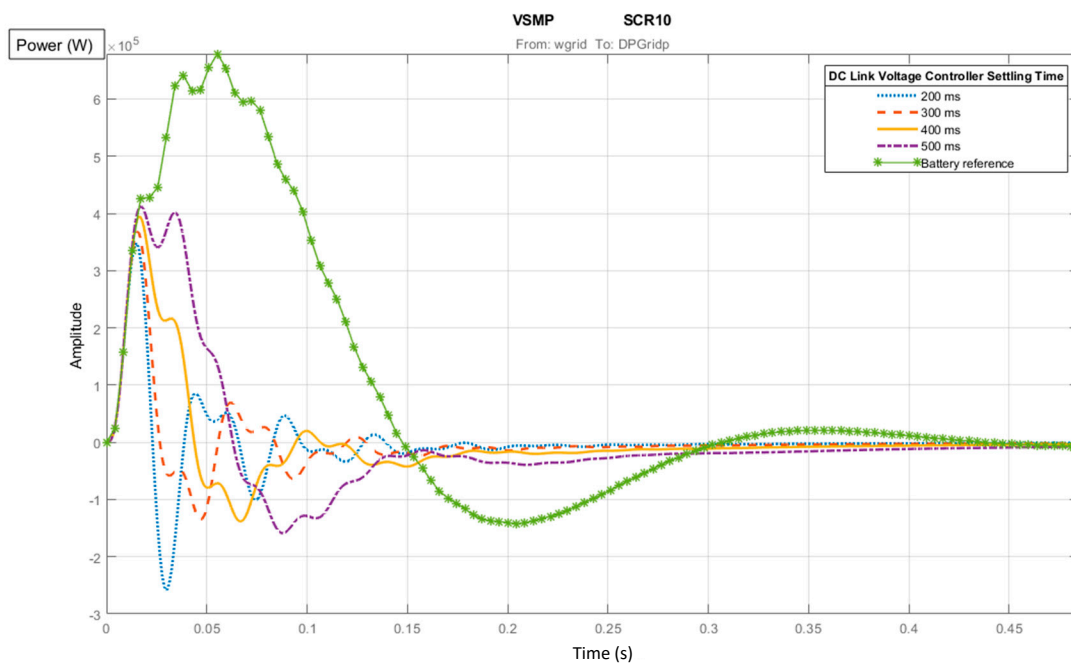

Figure 20. Step response showing effect of DC link controller bandwidth on VSM frequency response.

Figure 19 indicates a larger degradation of the inertial performance as the speed of the controller was increased. Even with the slowest tuning of 500 ms (purple dash-dot), the performance across the range of inertial frequencies was decreased and the peak response was flattened with its frequency shifted up by 6 Hz. There was a very large difference from the ideal case across the range and the frequency at which the peak response occurred moved to around 25 Hz. The frequency of the peak response increased with controller speed, resulting in an instability when the settling time fell below 200 ms. This was thought to be due to the interaction with the peak at 50 Hz. It should be noted that in order to match the ideal response, the controller had to be tuned to a settling time of over

3 s. This essentially allowed for the inertial response to occur before the DC link controller reacted to restore the voltage, but this is too slow for deployment in a real system. Beyond 50 Hz, the tuning of the DC link controller had no effect on the output.

Looking at Figure 20 the negative impact of the DC link voltage controller is evident. The peak power responses were much lower than the ideal case and reduced steadily as the voltage controller gains were increased. The difference observed between the fastest (blue dotted) and slowest controllers (purple dash-dot) was 50 kW. The blue dotted trace exhibited more oscillatory behaviour than the slower-tuned controllers. This is thought to be due to the DC link controller and inertial response fighting against each other more aggressively. The same tests were conducted for the PVCCI to ensure the issue was not just a result of the VSM controller. The Bode plots can be viewed in Figure 21 and the response when subjected to a frequency step of 1 rads^{-1} is given in Figure 22.
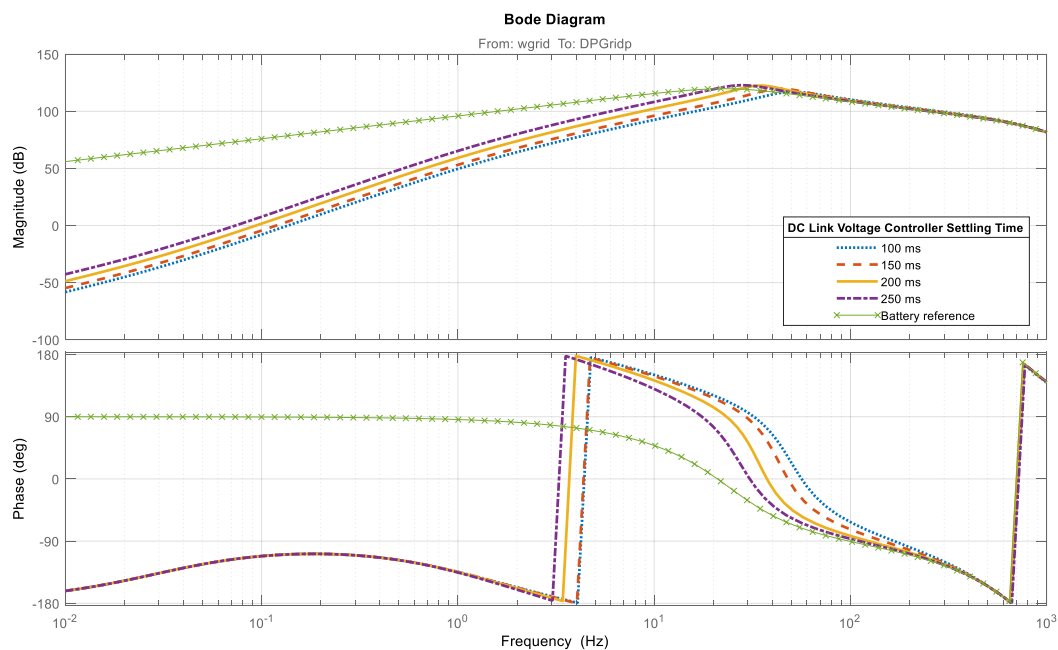

Figure 21. Bode plots showing the effect of the DC link controller bandwidth on the PVCCI frequency response.
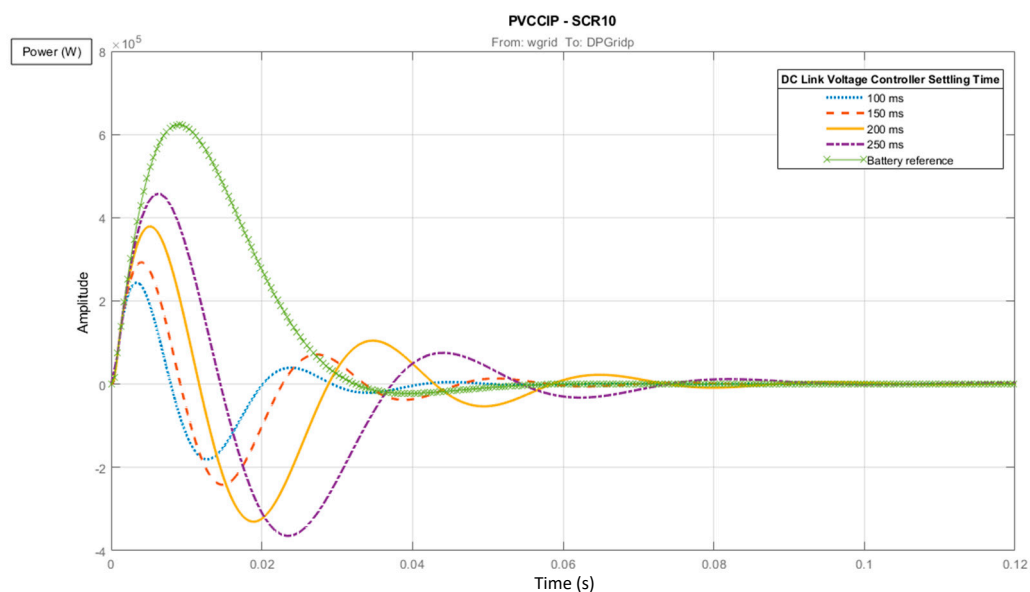

Figure 22. Step showing the effect of the DC link controller bandwidth on the PVCCI frequency response.

From Figure 21, the PVCCI exhibited a similar degradation in inertial performance as the VSM controller when the speed of the DC link voltage controller was increased. Note that the same proportional and integral gains were used for both the PVCCI and VSM; however, in the case of the PVCCI, the DC link voltage settling time was faster. The PVCCI gain response did not contain a peak in the inertial frequency range and the frequency of the peak response did not shift as noticeably as with the VSM controller. However, there was a clear reduction in performance across the entire range of inertial frequencies.

Figure 22 presents a smoother reaction for the PVCCI than that of the VSM controller. This made it easier to view the reduction in peak power response during a frequency event. A large change was again observed between the ideal-battery cases and the wind-turbine-connected cases. In the case of the PVCCI, the difference between the peak power response for an increasing DC link voltage controller speed was larger than that of the VSM controller: approximately 200 kW for the PVCCI and 50 kW for the VSM controller. The settling time for the event was also much smaller for the PVCCI than the VSM, but this was due to the controller structure rather than the DC link voltage control.

The outputs shown in Figures 19–22 were for a system where the generator-side converter was unaware of the event; there was no feedforward to the generator controller to extract energy from the turbine. The feedforward discussed in Section 2.2 was then enabled to determine whether the degradation in inertial performance could be improved by reducing the deviation of the DC link. Figure 23 shows a bode plot of the PVCCI system with a response in mechanical speed, DC link voltage and network power for a network frequency step of 1 rads^{-1} given in Figure 24. Figure 25 presents a bode plot of the VSM system and Figure 26 illustrates the VSM response in mechanical speed, DC link voltage and network power for a network frequency step of 1 rads^{-1}.
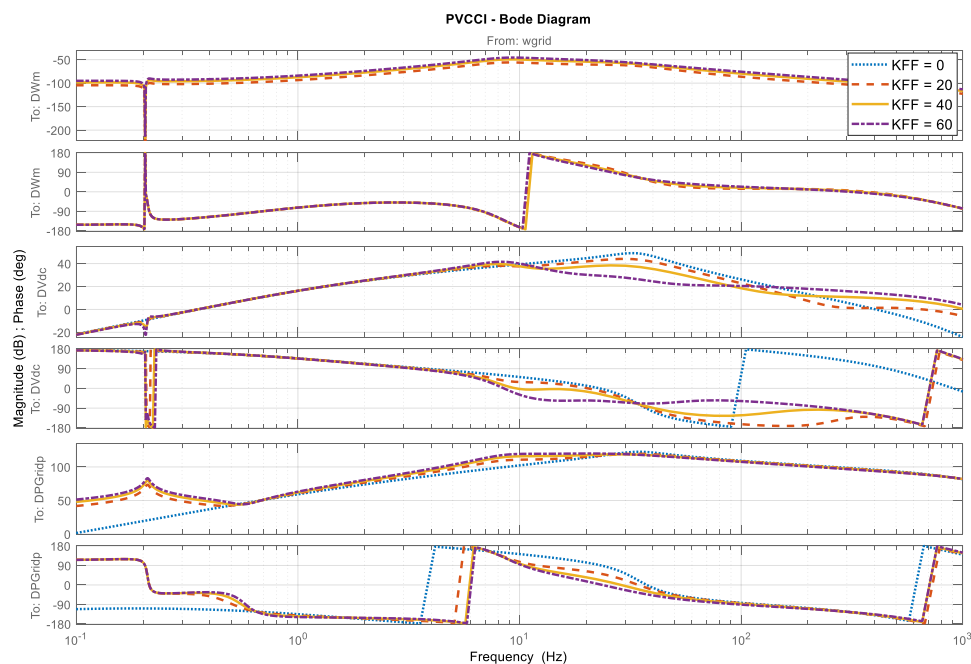

Figure 23. PVCCI Bode plots showing the effect of inertia feedforward to the generator.
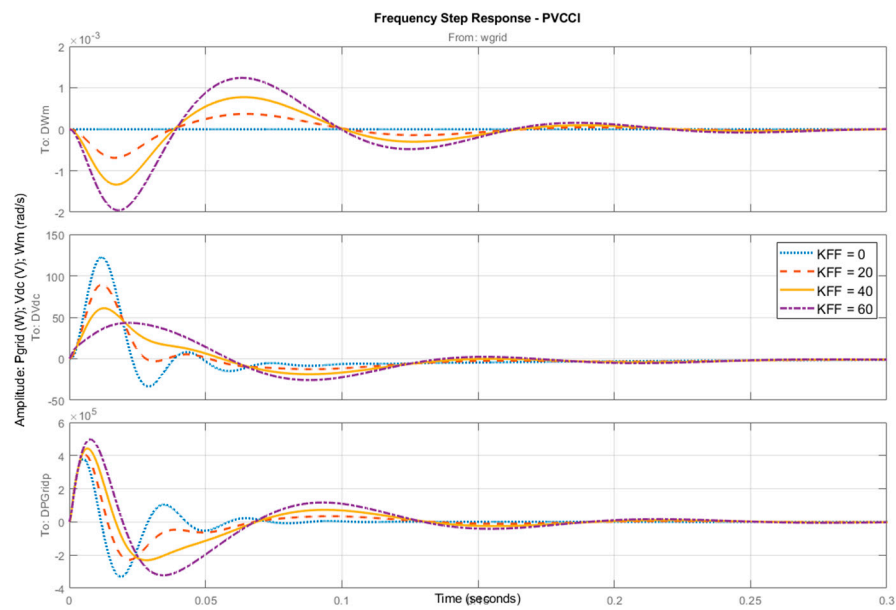
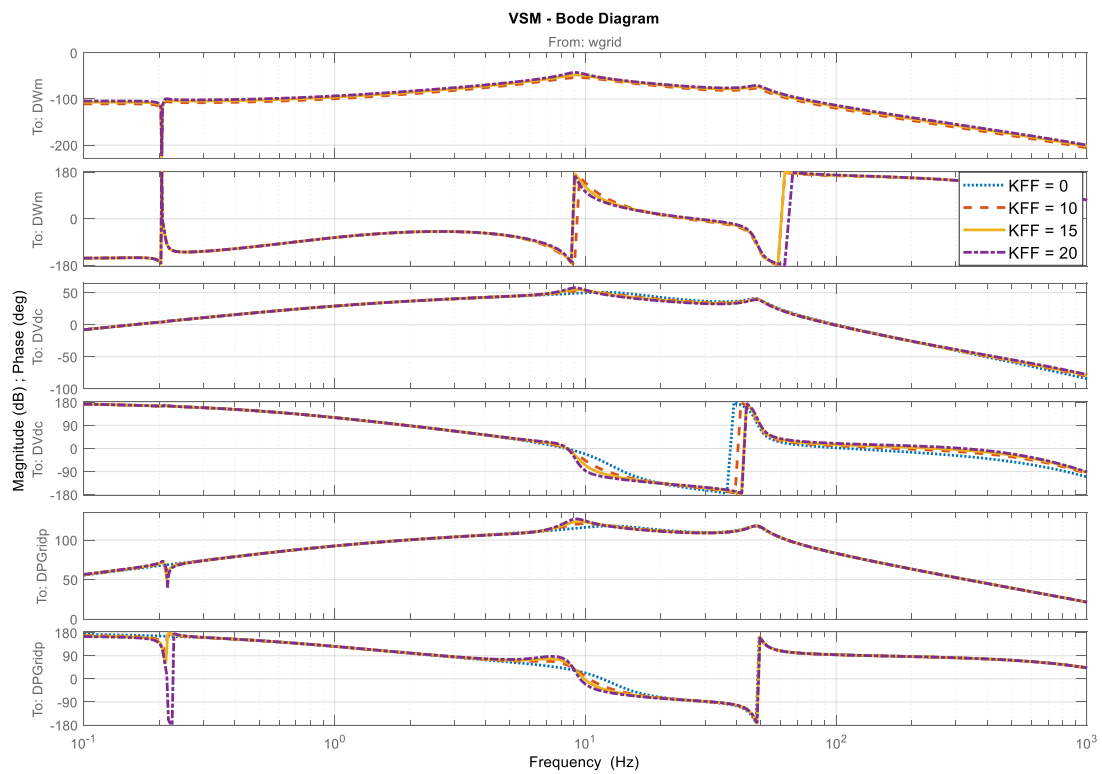**Figure 24.** PVCCI frequency step response with feedforward to the generator.

Figure 25. VSM Bode plot showing the effect of inertia feedforward to the generator.
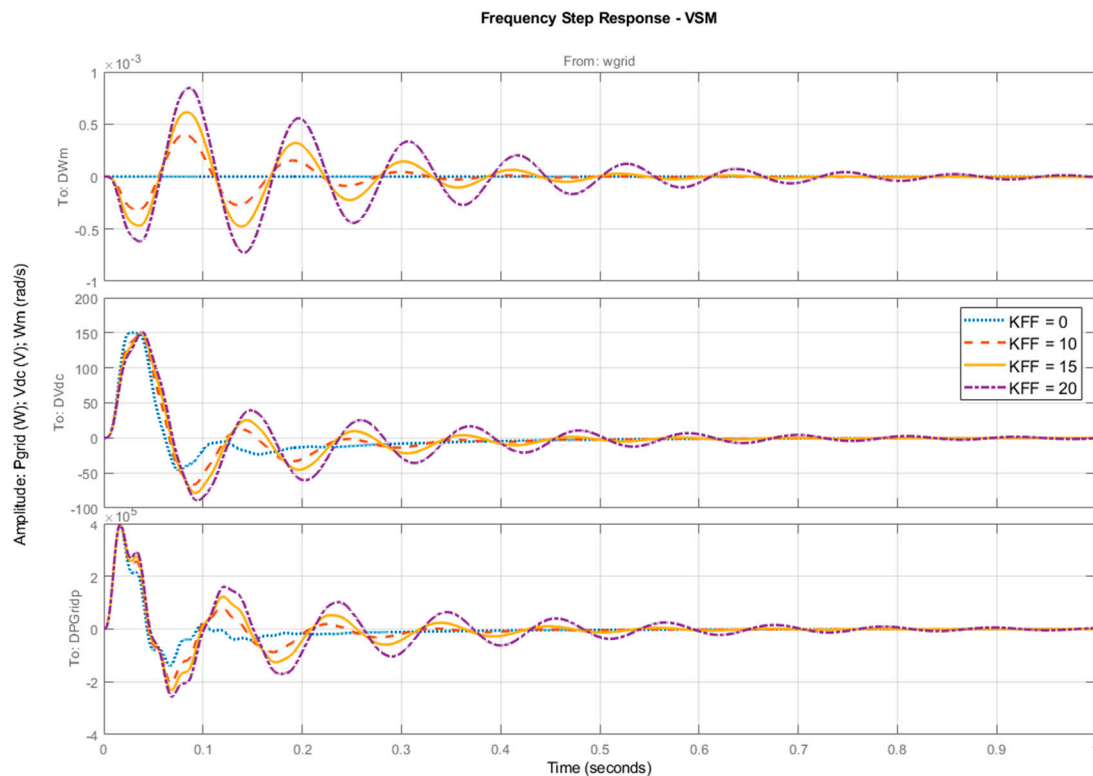
Figure 26. PVCCI Bode plot showing the effect of inertia feedforward to the generator.

Looking at frequency range of 0.1–1 Hz in Figure 23, when the power feedforward was included, the generator drivetrain dynamics were no longer decoupled from the grid power under frequency events. This is evident from the peak around 0.2 Hz in the network power magnitude response, which was not present when the feedforward gain (KFF) was 0 (blue dotted trace). In addition to this, the gain response was larger for an increasing feedforward gain across the range of inertial frequencies, indicating an improvement in the inertia response of the network converter. Another peak can be seen forming at around 9 Hz in the gain response for the mechanical speed, DC link voltage and network power as the feedforward gain was increased. The effect of this can be seen in Figure 24. As the feedforward gain increased, the active power response of the network converter increased, while the DC link voltage deviation decreased. This suggests an improvement in performance. However, the drivetrain experienced a larger oscillation magnitude as the inertial performance was enhanced. The frequency of the ringing matched the peak formed at around 9 Hz in Figure 23. If the feedforward gain was increased to more than 60, the ringing worsened and the DC link voltage deviation began to increase. This result was again observable when the VSM controller was used.

From Figure 25, the addition of the feedforward term had little effect on the inertial performance of the VSM controller over the range of inertial frequencies. A similar peak that was observed for the PVCCI in Figure 23 was seen in the network power gain response around 9 Hz for all three outputs. However, in the case of the VSM controller, the difference between the lowest (dotted blue) and highest (dot-dash purple) trace was less than that of the PVCCI. It should be noted that the feedforward gains were lower for the VSM controller than the PVCCI to maintain stability. This is easily explained by observing Figure 26. The oscillation at around 9 Hz was more prolonged for the VSM controller even though the feedforward gains were lower. Furthermore, there were no observable differences between the initial peaks of the network converter power response. The amplitude of the oscillation in the drivetrain was smaller but the damping was lower for the VSM controller than the PVCCI. The deviation in the DC link voltage was also unchanged, indicating that the inertial performance was not improved despite placing more strain on the drivetrain.

4. Discussion

The ability of the network side converter to respond to frequency events is important for grid stability in an inverter-dominant network. When the DC link controller is added on the network side, the inertial response performance is reduced, degrading network stability. The inertial response also limits how fast the DC link voltage control can be tuned as the interaction worsens with increased control speed. However, it could be argued that since the generator converter does not react to the frequency event, the energy is not being extracted from the turbine but instead from the DC link itself. By using an inertia feedforward term, this problem can be mitigated for the PVCCI as the generator increases power output by slowing the turbine during frequency events, thus reducing the overall deviation of the DC link. However, if the network frequency deviation is sufficiently fast, it can cause large, almost instantaneous changes in torque, which cause the drivetrain to oscillate. This is exacerbated when the feedforward gain is large as the torque step is greater. This drivetrain oscillation feeds into the DC link and can cause further issues with the network converter. The problem is more evident with the VSM controller as the control structure is more susceptible to DC link voltage ringing.

The easiest way to avoid the interaction is to move the DC link voltage control responsibility to the generator side converter. This allows for the network side converter to respond freely to frequency events. The DC link control then slows the turbine, extracting energy from the rotor and preventing DC link voltage perturbations. However, an interaction occurs between the drivetrain active damping and the DC link voltage control. The damping of torsional vibrations relies on the altering of electromagnetic torque via the injection or absorption of the q-axis current. The DC link controller opposes the action of the active damping, preventing the smoothing of mechanical oscillations. This could lead to extra strain being placed on drivetrain components.

Another possible solution is to include a form of energy storage [33], essentially shifting the system architecture towards that of an ideal battery connected system. The optimal sizing and location of this energy storage requires further study. It would still be possible to use the inertia included within the turbine to charge the energy storage system (ESS) but this would occur during steady-state conditions, therefore preventing the interactions observed within this paper. Without ESS, the selection of the DC link voltage control location will either harm the network stability or cause extra strain on the drivetrain components, limiting the effect of the inertia support.

Several differences can be observed between the grid-following (PVCC, PVCCI) and grid-forming controller (VSM). First, when connected to an ideal energy source, the SCR had a larger effect on the PVCCI than the VSM controller. The gain response for the grid-following controller deviated greatly for a changing SCR throughout the range of inertial frequencies, with a large resonant peak forming as the SCR decreased. This indicates that grid forming controllers may offer an improvement over traditional control strategies in weak grids. However, if Section 3.4 is considered, the VSM controller was more susceptible to DC link voltage fluctuations, with large vibrations observed throughout the system. The grid following the PVCCI coped better with the interaction by successfully dampening the oscillations. This led to an improved inertial response that was not obtainable using the VSM controller. A final issue relates to the converter sizing. The VSM controller has no inherent current limiting. Therefore, if the converter was operating near maximum power when a frequency event occurred, the controller would attempt to contribute more current and damage the devices. One option in this case is to oversize the converter to manage such issues. However, this would depend on the cost and frequency at which the converter is expected to exceed the current limits. The PVCCI controller contains an inner loop current controller, making it easier to prevent this problem.

In normal conditions, the rate of change of frequency would be slower. This may have an impact on the interaction between the DC link controller and the inertia provision or damping of mechanical vibrations. Further study is required to characterise this. Conducting further tests on real hardware is challenging, especially using real wind turbines due to time and cost constraints. Limited studies are available by applying grid-forming control to a wind park [34]. However, future work could

look at using hardware-in-the-loop with real converters and a simulated plant to further characterise interactions while introducing more complex variables.

5. Conclusions

This paper presents analysis of three wind-turbine-connected network converter control topologies, including generator and drivetrain dynamics: power voltage current control, power voltage current control with inertia emulation and a virtual synchronous machine. The effect of DC link voltage control was studied on both the network- and generator-side converters. The linearised small-signal models were constructed to analyse the response of each system to network frequency events.

The control of the DC link voltage directly impaired the ability of a converter to react to frequency events. In the case of the network side converter, this mainly affected the inertia response. As the converter reacted to frequency events by injecting or absorbing power, the DC link controller opposed it. The inertial performance degraded as the DC link controller gains increased. It was possible to reduce the DC link voltage deviation when an inertia-based feedforward was added to the generator converter. However, this increased the presence of the drivetrain dynamics in the DC link, consequently harming network stability as the control attempted to compensate. In the case of the generator-side converter, this mainly affected the drivetrain damping in a similar way. The controller with the larger gain tended to dominate the interaction. However, if both gains were sufficiently large, neither controller dominated and the oscillation persisted at a new frequency. These effects could be mitigated by increasing the capacity of the DC link or including another appropriate form of energy storage.

References

1. Department for Business energy & Industrial Strategy. *UK National Energy and Climate Plan (NECP)*; UK Government: London, UK, 2019.
2. Department for Business, Energy and Industrial Strategy. *UK Energy Statistics, Q1 2019*; UK Government: London, UK, 27 June 2019.
3. Tielens, P.; van Hertem, D. Grid Inertia and Frequency Control in Power Systems with High Penetration of Renewables. In Proceedings of the Young Researchers Symposium in Electrical Power Engineering, Delft, The Netherlands, 16–17 April 2012.
4. Wind Europe. *Wind Energy in Europe in 2018—Trends and Statistics*; Wind Europe: Brussels, Belgium, 2019.
5. Erlich, I.; Korai, A.; Shewarega, F. Study on the minimum share of conventional generation units required for stable operation of future converter-dominated grids. In Proceedings of the 2018 IEEE Power & Energy Society General Meeting (PESGM), Portland, OR, USA, 5–10 August 2018.
6. Yu, M.; Roscoe, A.J.; Dysko, A.; Booth, C.D.; Ierna, R.; Zhu, J.; Urdal, H. Instantaneous penetration level limits of non-synchronous devices in the British power system. *IET Renew. Power Gener.* **2017**, *11*, 1211–1217. [CrossRef]
7. Zhu, J.; Booth, C.; Adam, G.; Roscoe, A.; Bright, C.G. Inertia emulation control strategy for VSC-HVDC transmission systems. *IEEE Trans. Power Syst.* **2012**, *28*, 1277–1287. [CrossRef]

8.   Morren, J.; Pierik, J.; de Haan, S.W.H. Inertial response of variable speed wind turbines. *Electr. Power Syst. Res.* **2006**, *76*, 980–987. [CrossRef]

9.   Serban, I.; Petrea, C. Microgrid control based on a grid-forming inverter operating as virtual synchronous generator with enhanced dynamic response capability. *Int. J. Electr. Power Energy Syst.* **2017**, *89*, 94–105. [CrossRef]

10. Mandrile, F.; Carpaneto, E.; Bojoi, R. Grid-Tied Inverter with Simplified Virtual Synchronous Compensator for Grid Services and Grid Support. In Proceedings of the IEEE Energy Conversion Congress and Exposition, Baltimore, MD, USA, 29 September–3 October 2019.

11. Zhao, M.; Yin, H.; Xue, Y.; Zhang, X.-P. The Impact on Power System with Wind Integration from Multiple Virtual Synchronous Machines. In Proceedings of the IEEE International Conference on Systems, Man and Cybernetics, Bari, Italy, 6–9 October 2019.

12. L. Torres, M.A.; C. Lopes, L.A.; T. Morán, L.A.; C. Espinoza, J.R. Self-Tuning Virtual Synchronous Machine: A Control Strategy for Energy Storage Systems to Support Dynamic Frequency Control. *IEEE Trans. Energy Convers.* **2014**, *29*, 833–840. [CrossRef]

13. Hogan, D.J.; Gonzalez-Espin, F.; Hayes, J.G.; Lightbody, G.; Albiol-Tendillo, L.; Foley, R. Virtual Synchronous-Machine Control of Voltage-Source Converters in a Low-Voltage Microgrid. In Proceedings of the 18th European Conference on Power Electronics and Applications, Karlsruhe, Germany, 5–9 September 2016.

14. D'Arco, S.; Suul, J.A.; Fosso, O.B. Small-Signal Modelling and Parameteric Sensitivity of a Virtual Synchronous Machine. In Proceedings of the Power Systems Computation Conference, Wroclaw, Poland, 18–22 August 2014.

15. Chen, Y.; Hesse, R.; Turschner, D.; Beck, H.-P. Improving the Grid Power Quality Using Virtual Synchronous Machines. In Proceedings of the International Conference on Power Engineering, Energy and Electrical Drives, Torremolinos (Malaga), Spain, 11–13 May 2011.

16. Virtual Synchronous Machines—Classification of Implementations and Analysis of Equivalence to Droop Controllers for Microgrids. In Proceedings of the IEEE Grenoble Conference, Grenoble, France, 16–20 June 2013.

17. D'Arco, S.; Suul, J.A.; Fosso, O.B. A Virtual Synchronous Machine implementation for distributed control of power converters in SmartGrids. *Electr. Power Syst. Res.* **2015**, *122*, 180–197. [CrossRef]

18. Van Wesenbeeck, M.P.N.; de Haan, S.W.H.; Varela, P.; Visscher, K. Grid Tied Converter with Virtual Kinetic Storage. In Proceedings of the IEEE Bucharest Power Tech Conference, Bucharest, Romania, 28 June–2 July 2009.

19. Torres, M.; Lopes, L.A.C. Virtual Synchronous Generator Control in Autonomous Wind-Diesel Power Systems. In Proceedings of the IEEE Electrical Power & Energy Conference, Montreal, QC, Canada, 22–23 October 2009.

20. Vassilakis, A.; Kotsampopoulos, P.; Hatziargyriou, N.; Karapanos, V. A Battery Energy Storage Based Virtual Synchronous Generator. In Proceedings of the IREP Symposium—Bulk Power System Dynamics and Control, Rethymnon, Greece, 25–30 August 2013.

21. He, W.; Yuan, X.; Hu, J. Inertia provision and estimation of PLL-based DFIG wind turbines. *IEEE Trans. Power Syst.* **2016**, *31*, 510–521. [CrossRef]

22. Ramtharan, G.; Jenkins, N.; Anaya-Lara, O.; Bossanyi, E. Influence of Rotor Structural Dynamics Representations on the Electrical Transient Performance of FSIG and DFIG Wind Turbines. *Wind Energy* **2007**, *10*, 293–301. [CrossRef]

23. Muyeen, S.M.; Ali, M.H.; Takahashi, R.; Murata, T.; Tamura, J.; Tomaki, Y.; Sakahara, A.; Sasano, E. Comparative study on transient stability analysis of wind turbine generator system using different drive train models. *IET Renew. Power Gener.* **2007**, *1*, 131–141. [CrossRef]

24. Alizadeh, O.; Yazdani, A. A Strategy for Real Power Control in a Direct-Drive PMSG-Based Wind Energy Conversion System. *IEEE Trans. Power Deliv.* **2013**, *28*, 1297–1305. [CrossRef]

25. Geng, H.; Xu, D.; Wu, B.; Yang, G. Active Damping for PMSG-Based WECS With DC-Link Current Estimation. *IEEE Trans. Ind. Electron.* **2011**, *58*, 1110–1119. [CrossRef]

26. Mendes, V.F.; Matos, F.F.; Liu, S.Y.; Cupertino, A.F.; Pereira, H.A.; de Sousa, C.V. Low Voltage Ride-Through Capability Solutions for Permanent Magnet Synchronous Wind Generators. *Energies* **2016**, *91*, 59. [CrossRef]

27. Geng, H.; Xu, D.; Wu, B.; Yang, G. Active damping for torsional vibrations in PMSG based WECS. In Proceedings of the 2010 Twenty-Fifth Annual IEEE Applied Power Electronics Conference and Exposition (APEC), Palm Springs, CA, USA, 21–25 Febuary 2010.

28. Harnefors, L.; Nee, H.-P. Model-based current control of AC machines using the internal model control method. *IEEE Trans. Ind. Appl.* **1998**, *34*, 287–293. [CrossRef]

29. Almeida, R.G.; Castronuovo, E.D.; Lopes, J.A.P. Optimum generation control in wind parks when carrying out system operator requests. *IEEE Trans. Power Syst.* **2006**, *21*, 718–725. [CrossRef]

30. Sanjari, M.J.; Gharehpetian, G.B. Unified framework for frequency and voltage control of autonomous microgrids. *IET Gener. Transm. Distrib.* **2013**, *7*, 965–972. [CrossRef]

31. Egea-Alvarez, A.; Fekriasl, S.; Hassan, F.; Gomis-Bellmunt, O. Advanced Vector Control for Voltage Source Converters Connected to Weak Grids. *IEEE Trans. Power Syst.* **2015**, *30*, 3072–3081. [CrossRef]

32. Zhang, L. Modeling and Control of VSC-HVDC Links Connected to Weak AC Systems. Ph.D. Dissertation, KTH, Stockholm, Sweden, 2010.

33. Ma, Y.; Cao, W.; Yang, L.; Wang, F.; Tolbert, L. Virtual synchronous generator control of full converter wind turbines with short-term energy storage. *IEEE Trans. Ind. Electron.* **2017**, *64*, 8821–8831. [CrossRef]

34. Roscoe, A.; Brogan, P.; Elliot, D.; Knueppel, T.; Gutierrez, I.; Campion, J.-C.P.; Da Silva, R. Practical Experience of Operating a Grid Forming Wind Park and its Response to System Events. In Proceedings of the 18th Interational Wind Integration Workshop, Dublin, Ireland, 16–18 October 2019.